CHALMERS
UNIVERSITY OF TECHNOLOGY

Experimentally Validated Inverse design of Multi-Property Fe-Co-Ni alloys

Citation for the original published paper (version of record):
Padhy, S., Chaudhary, V., Lim, Y. et al (2024). Experimentally Validated Inverse design of Multi-Property Fe-Co-Ni alloys. iScience, 27(5). http://dx.doi.org/10.1016/j.isci.2024.109723

iScience

CellPress
OPEN ACCESS

Article

Experimentally validated inverse design of multi-property Fe-Co-Ni alloys

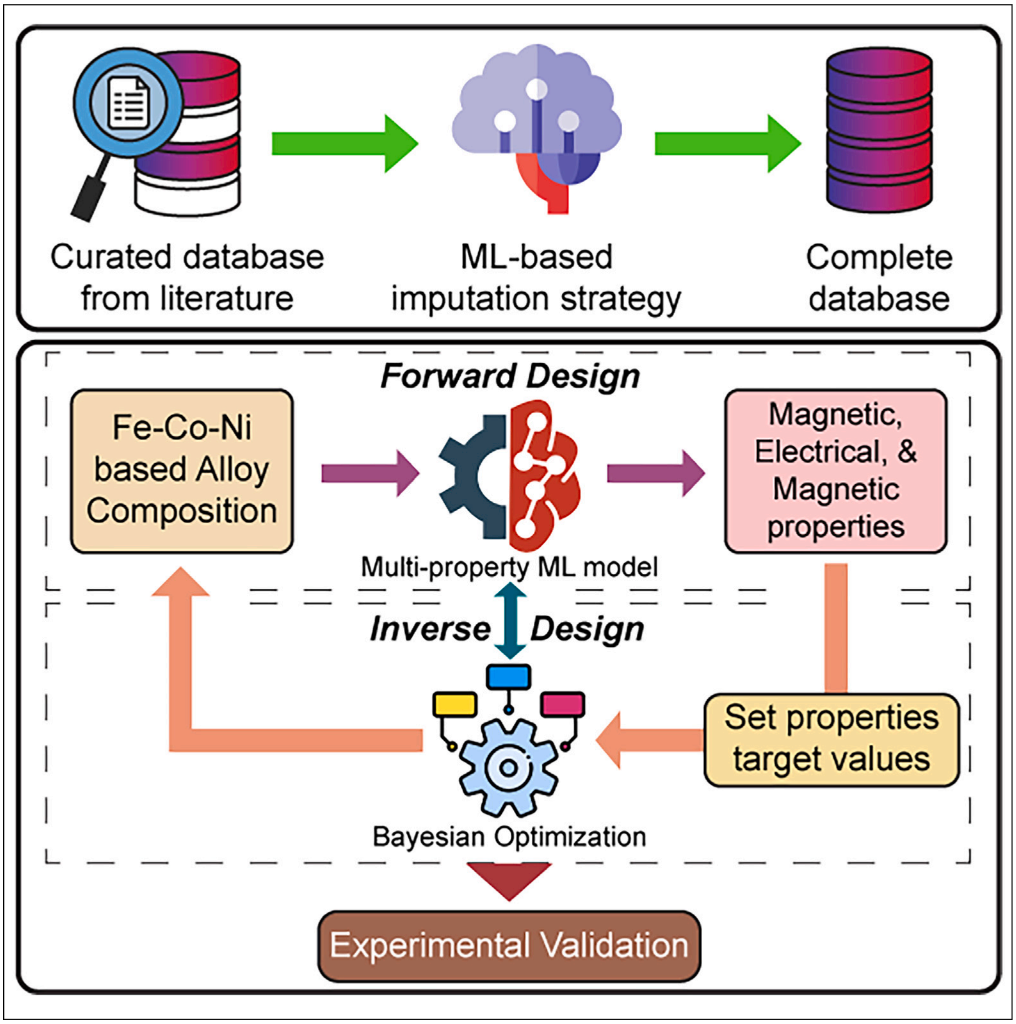

Shakti P. Padhy, Varun Chaudhary, Yee-Fun Lim, Ruiming Zhu, Muang Thway, Kedar Hippalgaonkar, Raju V. Ramanujan

kedar@ntu.edu.sg (K.H.)
ramanujan@ntu.edu.sg (R.V.R.)
varunc@chalmers.se (V.C.)

Highlights

A machine learning framework for multi-property optimized Fe-Co-Ni alloy design

Predictive models and multi-objective Bayesian optimization predict promising alloys

Experimental validation confirms superior multi-property performance of the alloys

$Fe_{66.8}Co_{28}Ni_{5.2}$ and $Fe_{61.9}Co_{22.8}Ni_{15.3}$ are the identified alloy compositions

Padhy et al., iScience *27*, 109723
May 17, 2024 © 2024 The Authors. Published by Elsevier Inc.
https://doi.org/10.1016/j.isci.2024.109723

iScience

CellPress
OPEN ACCESS

Article

Experimentally validated inverse design of multi-property Fe-Co-Ni alloys

Shakti P. Padhy,[1,2] Varun Chaudhary,[3,*] Yee-Fun Lim,[4,5] Ruiming Zhu,[1] Muang Thway,[1] Kedar Hippalgaonkar,[1,4,*] and Raju V. Ramanujan[1,6,*]

SUMMARY

This study presents a machine learning (ML) framework aimed at accelerating the discovery of multi-property optimized Fe-Ni-Co alloys, addressing the time-consuming, expensive, and inefficient nature of traditional methods of material discovery, development, and deployment. We compiled a detailed heterogeneous database of the magnetic, electrical, and mechanical properties of Fe-Co-Ni alloys, employing a novel ML-based imputation strategy to address gaps in property data. Leveraging this comprehensive database, we developed predictive ML models using tree-based and neural network approaches for optimizing multiple properties simultaneously. An inverse design strategy, utilizing multi-objective Bayesian optimization (MOBO), enabled the identification of promising alloy compositions. This approach was experimentally validated using high-throughput methodology, highlighting alloys such as $Fe_{66.8}Co_{28}Ni_{5.2}$ and $Fe_{61.9}Co_{22.8}Ni_{15.3}$, which demonstrated superior properties. The predicted properties data closely matched experimental data within 14% accuracy. Our approach can be extended to a broad range of materials systems to predict novel materials with an optimized set of properties.

INTRODUCTION

Material innovation has often been the key to advances in technology. Multi-component alloys, polymers, composites, semiconductors, superconductors, and biocompatible materials have promoted a revolution in construction, transportation, energy, bioengineering, microelectronics, and space technologies.[1,2] Research and development in the field of materials science can be divided into four major paradigms: empirical trial and error methods, theoretical models and laws, computational simulations, and data-driven science.[3–6] The first three paradigms are experiment, theory, and computation and constitute the traditional methodology of discovering and developing materials. From research to applications, traditional methods typically take decades, require high expenditures, are highly inefficient, and usually do not result in the best composition for a given application.[5,7–9] On the other hand, data-driven science using machine learning (ML) of mined material data integrated with high-throughput experiments and computing can be used to design and discover new materials, and a vast space of materials and processing conditions can be studied with minimum time and cost.[6,7,9–21]

One such important class of materials are alloys used in essential components of electro-magnetic energy conversion devices, for e.g., electrical motors, generators, transformers, inductors, actuators, magnetic-MEMS, and magnetic recording media.[2,22–25] Due to increased global electricity consumption, e.g., an increase of 1.7% from 2018 to 2019[26] and a projected growth rate of 3–4% per annum from 2019 to 2050,[27] there is an urgent need for developing energy-efficient electrical technologies. Next-generation superior alloys hold the key to developing high efficiency, low cost, and compact devices that are also suitable to operate in extreme service conditions, for e.g., high frequency rotating electrical machines.[23,28–31] Additionally, an improvement of only 1% in the efficiency of electric motors will reduce global power consumption by 94.5 TW-hours and carbon dioxide emissions by 60 million metric tons.[32,33]

However, there is no single commercial magnetic alloy that is commercially used with optimized multiple properties for current technological applications. Recently, a novel alloy ($Fe_{32.6}Ni_{27.7}Co_{27.7}Ta_5Al_7$) was reported with a high tensile strength of 1336 MPa and a low coercivity of 78 A/m.[34] This combination of properties was achieved by developing precipitates, enriched in nickel, tantalum, and aluminum with a controlled size and by tuning the particle/matrix interfacial coherency.[34,35] The precipitates developed in these alloys impeded dislocation motion, thereby improving strength, and did not significantly increase the pinning effect of the precipitates on the domain wall movement, maintaining low coercivity. This phenomenon was achievable due to the use of various constituent elements in the alloy system, which

---

[1] School of Materials Science and Engineering, Nanyang Technological University, 50 Nanyang Avenue, Singapore 639798, Republic of Singapore
[2] Department of Materials Science and Engineering, University of Tennessee, Knoxville, TN 37996, USA
[3] Industrial and Materials Science, Chalmers University of Technology, SE-41296 Gothenburg, Sweden
[4] Institute of Materials Research and Engineering (IMRE), Agency for Science, Technology and Research (A*STAR), 2 Fusionopolis Way, Singapore 138634, Republic of Singapore
[5] Institute of Sustainability for Chemicals, Energy and Environment (ISCE2), Agency for Science Technology and Research (A*STAR), 1 Pesek Road, Jurong Island, Singapore 627833, Republic of Singapore
[6] Lead contact
*Correspondence: kedar@ntu.edu.sg (K.H.), ramanujan@ntu.edu.sg (R.V.R.), varunc@chalmers.se (V.C.)
https://doi.org/10.1016/j.isci.2024.109723

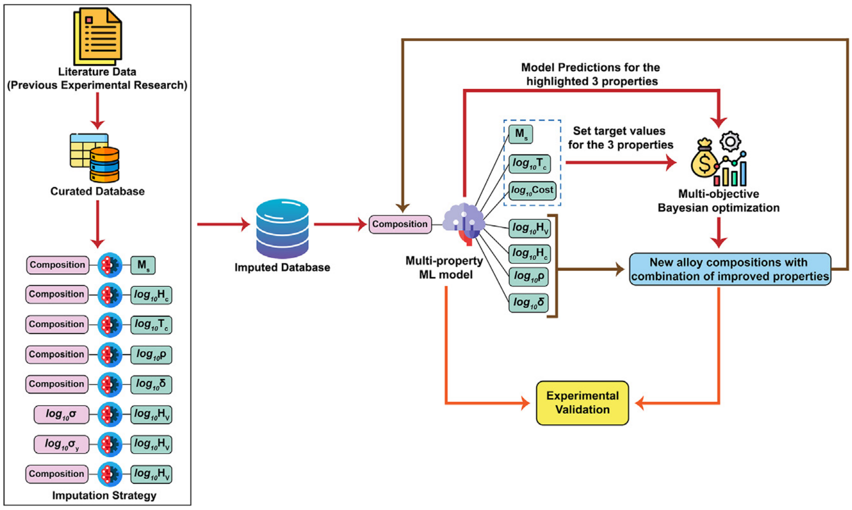

Figure 1. Overview of the work

Database Curation, Machine Learning (ML) based imputation strategy used to complete the database, multi-property ML regression model [Forward Design of alloys], Multi-objective Bayesian optimization (MOBO) [Inverse Design of alloys], and the Experimental Validation of forward design and predicted new alloy composition from inverse design.

facilitates a balance of multiple properties.[35] However, the alloy exhibited lower saturation magnetization than those of the best soft magnetic materials because the precipitates formed were paramagnetic in nature.[35] Therefore, the right choice of the principal constituent elements and their content in a multi-component alloy system is essential in developing next-generation magnetic alloys.

In this work, Fe-Co-Ni-based alloy compositions were chosen as the three elements are ferromagnetic in nature and certain alloy compositions can potentially provide a better combination of properties. Binary alloys of these ferromagnetic elements exhibit certain excellent properties. For e.g., $Ni_{78}Fe_{22}$ (78–Permalloy) and $Ni_{78}Fe_{17}Mo_5$ (Supermalloy) exhibit high permeability (μ) and low coercivity (H_c). Co exhibits the highest Curie temperature (T_c) of 1394 K, while $Fe_{65}Co_{35}$ exhibits the highest saturation magnetization (M_s) of 2.47 T followed by $Fe_{49}Co_{49}V_2$. On the other hand, Fe-Si alloys with 2–4.5 wt % Si exhibit low H_c, low magnetocrystalline anisotropy and high electrical resistivity (ρ).[2,22,23,36] The desired set of technical properties required for next-generation alloys for rotating electric machines include magnetic, electrical, and mechanical properties, e.g., high M_s, low H_c, high T_c, high μ, high ρ, high tensile (σ) and yield (σ_y) strength, high ductility (δ), and high hardness (H_V). Thus, multi-property optimization and new alloy compositions are required. Machine learning (ML) can reveal novel alloy compositions with optimized properties.

ML has been applied to alloy design mainly focusing on a single property,[13,14,37–40] and a few studies have been performed to optimize multiple properties.[8,41–47] In the present study, we collect multiple property data on Fe-Co-Ni alloys from the literature to create a curated database. We combined ML with Bayesian optimization (BO) to identify Fe-Co-Ni alloys with the desired multiple property set. The curated database contained gaps in the property data that were filled using an ML-based imputation technique. This imputed database was used to develop a multi-property ML model (forward design). Multi-objective BO (inverse design) was implemented to identify alloys with superior property sets. Both the forward and inverse design results were validated using experimental data obtained using a high-throughput methodology. The compositions, $Fe_{65.84}Co_{28.66}Ni_{5.5}$ and $Fe_{61.5}Co_{23.14}Ni_{15.35}$, revealed by BO, demonstrate high values of M_s, T_c, and H_V, moderately low values of H_c and moderately high values of ρ, a superior property set compared to conventional Fe-Co-Ni magnetic alloys. The strategy is shown in Figure 1. The proposed approach is applicable to a wide variety of multi-property optimization materials design problems.

METHODOLOGY

The *Python* programming language was used for exploratory data analysis, model building, and optimization. The *Pandas*[48–50] library was used to handle data. *Matplotlib*,[51] *seaborn*,[52] and *plotly*[53] libraries were used for plotting. *Keras*[54] from *TensorFlow*[55] library was used to implement Deep Neural Network (DNN) models, *XGBoost*[56] library was used to implement XGBoost Regression (XGBR), and *Scikit-Learn*[57] library was used for the rest of the models. For BO, *gp_minimize* from the *Scikit-Optimize*[58] library was implemented.

The Fe-Co-Ni-based alloy database along with the codes for database analysis, the eight imputation steps, multi-property models, multi-objective Bayesian optimization (MOBO), and plotting of experimental validation results is publicly available.[59]

Database Curation and analysis

A database of Fe-Co-Ni-based alloys (with the optional addition of other elements up to a combined at % less than 10) and their corresponding magnetic (M_s, H_c, T_c), electrical (ρ), and mechanical (σ, σ_y, δ, Vickers Hardness (H_V)) properties were collected from the literature. From thousands of publications and hundreds of handbooks describing Fe-Co-Ni-based alloy composition(s) and their properties, data was extracted from selected sources based on the criterion that two or more properties for the alloy composition were experimentally determined. For research publications, Clarivate Web of Science was used to search for articles with various search strings for the year range from 1900 to 2021. Further, relevant publications were selected for each search string by first screening various abstracts and then screening the publication for information related to Fe-Co-Ni-based alloys. Sources used for database building include:

(1) Books – *Ferromagnetism,*[60] *Magnetism and Magnetic Materials,*[61] *Bibliography of Magnetic Materials and Tabulation of Magnetic Transition Temperature*[62];
(2) Handbooks – *Powder Metallurgy Data Part 1: Metals and Magnets,*[63] *ASM Handbook Volume 2,*[64] *Handbook of Materials Selection*[65,66];
(3) Research/Review articles [67–80,81-112].

A total of 1208 data entries were curated from the above-mentioned references from text, tables, and graphical images. The information from graphical images were extracted using graph digitizing software such as Graph Grabber (v2.0.2, Quintessa Ltd., UK), Enguage Digitizer,[113] and Digitizer Tool of OriginPro 2020b (OriginLab Corporation, USA). The content of elements in the alloy composition was converted to atomic percentage (at. %). If the reported composition was in weight percentage (wt. %), it was converted to at.% before adding to the the database. The properties were converted to SI units, i.e., M_s in Tesla (T), H_c in Ampere/meter (A/m), T_c in Kelvin (K), ρ in Micro ohm centimeter ($\mu\Omega\cdot cm$), σ and σ_y in Megapascals (MPa), δ in %, and H_V in HV. Using the elemental content information and the individual element price,[114] overall raw material cost (US$/kg) for each alloy was calculated and added to the database. For database analysis, the distribution of the elements and properties was plotted. The Pearson correlation coefficients for each property versus the alloy composition as well as between the properties were calculated and plotted. Finally, the percentage of the property data filled in the database was calculated for each property.

Imputation strategy

An imputation strategy was developed to fill the empty cells in the properties columns so that the imputed database can be used to build a multi-property model mapping the composition to the properties. 12 different regression models were built, mapping the composition to each of the responses, by training on 80% of the available property data. These are Linear Regression (Linear), Ridge Regression (Ridge), Lasso Regression (Lasso), K-Nearest Neighbors Regression (KNNR), Support Vector Regression (SVR), Decision Tree Regression (DTR), Gradient Boosting Regression (GBR), Random Forest Regression (RFR), Extra Trees Regression (ETR), XGBoost Regression (XGBR), Deep Neural Network Regression with same number of units in all the hidden layers (DNNR_rectangle), and Deep Neural Network Regression with different number of units in the hidden layers (DNNR_random). The details of the hyperparameters optimization and model building are discussed in Section S2 *of* supplementary information. After all the models were built, the best model with the lowest mean-absolute error (MAE) for the testing data was selected for the imputation of that respective property column.[115] Those models also exhibited low root mean-squared error (RMSE) and high coefficient of determination (R^2).

For all the properties except $log_{10}H_V$, imputation was performed directly using the best model mapping from composition to the property as explained above. For $log_{10}H_V$, imputation was done in 3 steps.

(1) 12 regression models were built mapping from $log_{10}\sigma$ to $log_{10}H_V$. The model with the lowest MAE was chosen to fill up the empty cells in the $log_{10}H_V$ column for which σ values were reported in the literature but not the H_V values.
(2) 12 regression models were built mapping from $log_{10}\sigma_y$ to $log_{10}H_V$, the model with the lowest MAE was chosen to impute the $log_{10}H_V$ values for which σ_y were reported but not H_V.
(3) Using both the experimental and imputed $log_{10}H_V$ values, all the 12 regression models were built mapping from the composition to $log_{10}H_V$, the model with the lowest MAE was chosen for the imputation of the $log_{10}H_V$ column.

Multi-property model for the forward design of the multi-property alloy

The imputed database was next used to build multi-property predictive models mapping the composition to M_s, $log_{10}H_c$, $log_{10}T_c$, $log_{10}\rho$, $log_{10}\delta$, $log_{10}H_V$, and $log_{10}Cost$. Six ML models, i.e., RFR, ETR, neural network regression with 3 hidden layers (NNR_3layers), neural network regression with 4 hidden layers (NNR_4layers), DNNR_rectangle, and DNNR_random were deployed. The hyperparameters for each of the models are discussed in Section S3 *of* supplementary information. Futher, using the same hyperparameters, another set of six multi-property predictive models was built mapping the composition and Wen alloy features[38] to the 7 properties. Further, the MAE of all the different models were compared with each other to select one tree-based model and one neural network model with the lowest MAE as multi-property predictive models. These models were experimentally validated using 40 Fe-Co-Ni compositions which were synthesized and characterized in a high-throughput manner.

Multi-objective Bayesian optimization for inverse design of the multi-property alloy

To design alloy compositions possessing an optimum balance of properties using the multi-property model, the implementation of a robust and computationally low-cost optimization algorithm is required. In this work, Bayesian optimization (BO) is used for fast, low cost and effective global optimization of those objective functions which are expensive and time-consuming to evaluate, i.e., expensive black box functions.[116–119]

A Gaussian Process (GP) based BO was used to obtain the multi-property regression (MPR) model predictions closer to the target values. The global minima/maxima composition was determined from the defined search space of elements. BO uses prior and evidence knowledge to define a posterior distribution over function space. The function space is maximized/minimized at each step such that the expected maximum/minimum of the given model moves closer to the global maximum/minimum.[120] In this work, *gp_minimize* from *Scikit-Optimize* was used for BO which minimizes the defined objective function. The acquisition function set in *gp_minimize* was "EI," which denotes a negative expected improvement. The expected improvement determines the global maximum of the objective function, which is explained in Section S5 of supplementary information. Thus, a negative expected improvement finds the global minima of the objective function.

The objective function defined for the BO to design alloy composition containing only Fe, Co, and Ni is described by the equations later in discussion,

$$x_n = \frac{x}{\sum x} \times 100 \qquad \text{(Equation 1)}$$

$$x_{transformed} = StandardScaler(x_n) \qquad \text{(Equation 2)}$$

$$pred = MPR(x_{transformed}) \qquad \text{(Equation 3)}$$

$$objective = \sum w_i \times abs(target_i - pred_i), \; if \; target_i \neq Nan \qquad \text{(Equation 4)}$$

where x in Equation 1 is the compositional array containing at.% values of Fe, Co, Ni, and other elements determined by the BO algorithm from the defined ranges: Fe, Co, Ni $\in$ [0, 100] and other elements $\in$ [0, 0.001], x_n in Equation 1 is the normalized compositional array to always maintain the sum of at.% of elements at 100%, *StandardScaler* in Equation 2 is the standard scaling function used on the training set for building the MPR model, *pred* in Equation 3 is the array of predicted property values by the MPR model, w_i in Equation 4 are the weights for optimizing each property which were defined manually, *Nan* in Equation 4 stands for Not a number, and $target_i$ and $pred_i$ in Equation 4 are the set target value and MPR model predicted value of each property. The idea of using weights is to emphasize the optimization of the desired property set close to the desired target value compared to other property set. This would be useful for discovering the optimum alloy composition for a particular application.

Experimental validation of forward and inverse design

40 Fe-Co-Ni alloy compositions were prepared using high-throughput experimental scheme using high-throughput spark plasma sintering (SPS) of ball-milled alloy powders which is explained elsewhere.[112,121] The alloy powders were prepared via ball milling (Fritsch Pulverisette-7) of Fe, Co, and Ni powders (purity≥99.95%, Tosoh SMD Inc.) using tungsten carbide vials and balls. 10 mm diameter balls were used and the ball-to-powder ratio was maintained at 12:1. The bulk alloy samples were prepared via SPS (Fuji Electronic Industrial, SPS-211LX) in compositionally graded cylindrical samples by stacking ball-milled powders and sintering them for 15 min at 950°C, 40 MPa, at vacuum level less than 8 Pa. The composition was measured using an energy-dispersive X-ray spectrometer attached to the JEOL JSM-7800F-SEM. The magnetic properties were measured using a physical property measurement system (EverCool-II, QD). The Curie temperature was measured in an accelerated manner using a modified thermogravimetric analysis (TGA) by placing a magnet near the TGA pan.[109,112,121,122] The Vickers hardness and electrical resistivity were measured using a Vickers hardness tester (Future-Tech) and a four-point probe (4PP) tester (Keithlink), respectively. The *Cost* for these compositions was calculated, as described in Section database curation and analysis.

For the experimental validation of the forward design methodology, the 40 Fe-Co-Ni compositions were used in the selected tree-based model and neural network model to predict the property values. These predicted values were compared with the experimental values of the properties and the MAE for all the properties for both models were calculated.

For the experimental validation of the inverse design methodology, the predicted alloy compositions by BO for the set target values of the properties were plotted and compared using interactive ternary contour plots of the properties of 40 rapidly synthesized Fe-Co-Ni compositions. For the predicted compositions, the properties were predicted using the compositions in the model which was used in BO.

RESULTS AND DISCUSSION

Database curation and analysis

15 elements were present in the database, the distribution is shown in Figure 2A–2N. The elements are Fe, Co, Ni, V, Mo, Cr, Cu, Mn, C, W, Ta, Nb, Al, Ti, and Si. According to the distribution of Fe shown in Figure 2A, there are more than 250 alloys containing Fe between 46.33 at % and 52.67 at%. From the distribution of Co shown in Figure 2B, a similar number can be inferred. The compositions containing Ni are broadly distributed as shown in Figure 2C. From the distribution of V and Cu in Figures 2D and 2G the alloy composition containing V or Cu is usually ~2 at%. The 15 elements were considered as features for the multi-property ML model, as described in Table 1.

The distribution of properties is discussed in Section S1 *of* supplementary information. The values of all the properties except for M_s were converted to log_{10} scale to reduce the skewness in the data and to make different property values comparable to each other. The distribution of the modified properties and cost is shown in Figures 2O–2W. The skewness of the distribution of the log_{10} scale converted properties decreased compared to the distribution in Figure S1, except for T_c and *Cost*.

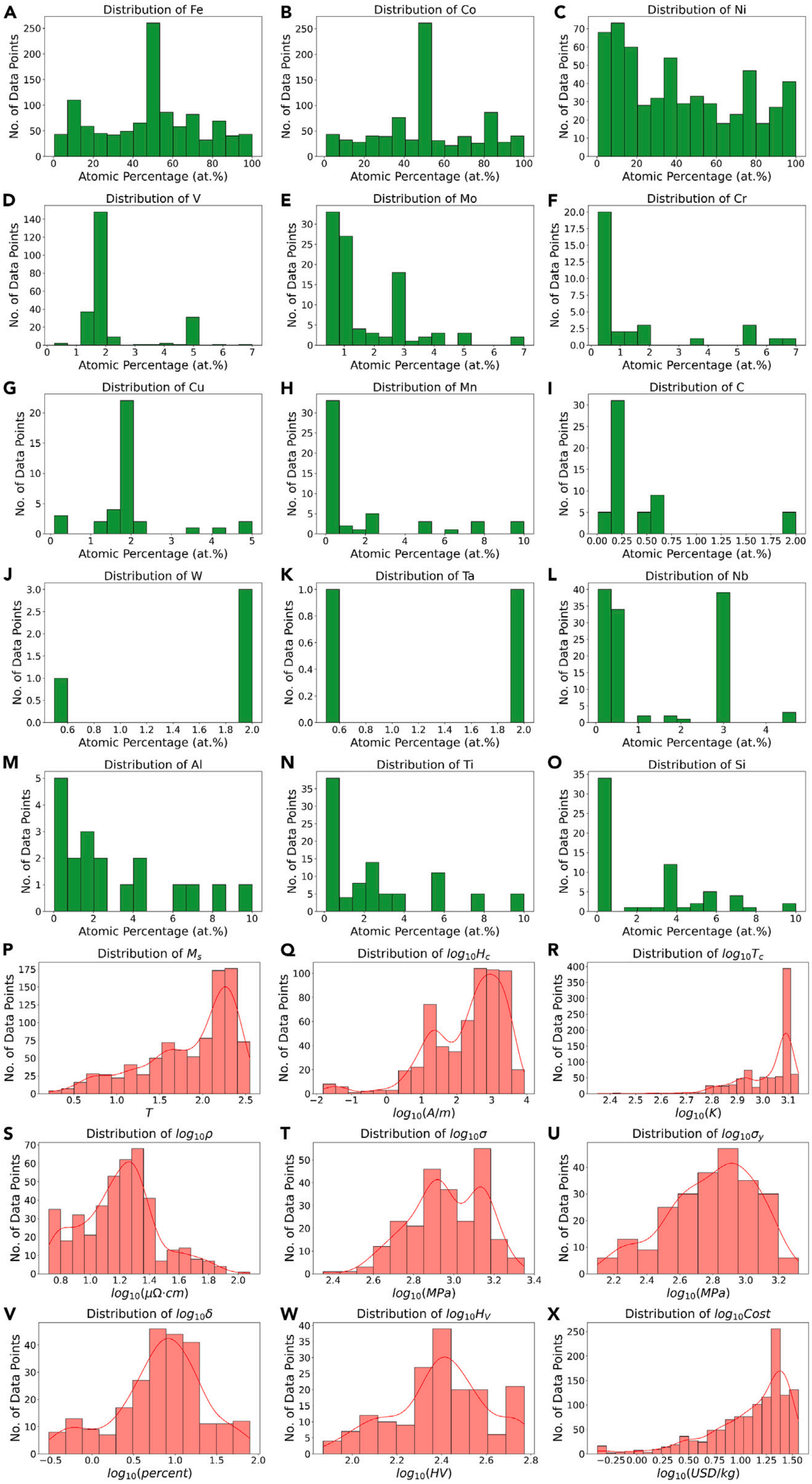

Figure 2. Distribution analysis of the database

Distribution of (A–O) 15 elements atomic percentage (at.%), (O–Q) magnetic properties (M_s, $log_{10}H_c$, $log_{10}T_c$), (R) electrical resistivity ($log_{10}\,\rho$), (S–V) mechanical properties ($log_{10}\,\sigma$, $log_{10}\,\sigma_y$, $log_{10}\,\delta$, $log_{10}H_V$), and (W) $log_{10}Cost$ in the database. In (P–X) the solid continuous lines are kernel density estimations which show the probability density function of the data entries for each property.

Table 1. Table of features and responses used for multi-property machine learning (ML) model

Features	Fe, Co, Ni, V, Mo, Cr, Cu, Mn, C, W, Ta, Nb, Al, Ti, Si
Responses	M_s, $log_{10}(H_c)$, $log_{10}(T_c)$, $log_{10}(\rho)$, $log_{10}(\delta)$, $log_{10}(H_V)$, and $log_{10}(Cost)$

To understand the relationship between the properties and alloy composition, the Pearson correlation coefficient was calculated for each property against all the 15 elements, as shown in Figure 3A. The Pearson correlation coefficient was also calculated between the properties to understand the inter-property relationships as shown in Figure 3B. From Figure 3A, it can be observed that the Fe content has a positive correlation with M_s while the Ni content has a negative correlation, implying that the addition of Fe will increase M_s whereas the addition of Ni will decrease M_s.[123] For $log_{10}H_c$, the Co content has a moderately positive correlation whereas the Ni content has a moderately negative correlation, which implies that the addition of Co increases $log_{10}H_c$, while the addition of Ni decreases $log_{10}H_c$. To support this inference, there have been studies in the past reporting that permalloy and moly permalloy exhibit lower coercivity values compared to Fe-Co alloys.[23,106,109,112]

The Co content has a positive correlation with $log_{10}T_c$ while the Ni content has a negative correlation, implying that the addition of Co increases $log_{10}T_c$, on the other hand, the addition of Ni decreases $log_{10}T_c$. This is consistent with the fact that Co has the highest T_c of 1394 K,[60,124] Ni has a much lower T_c of 631 K.[125] This change in T_c values can also be rationalized by the mean field model and the Bethe-Slater curve.[18,126] $log_{10}H_c$ has a positive linear correlation with $log_{10}T_c$, $log_{10}\sigma$, and $log_{10}\sigma_y$ (Figure 3B). The positive linear correlation between $log_{10}H_c$ and $log_{10}T_c$ can be attributed to an increase in Co content (Figure 3A).

Moreover, interestingly, Fe has a moderately negative correlation with $log_{10}\delta$ implying, with all other factors unchanged, δ decreases with an increase in Fe content. Further, V and C have a moderately positive correlation with $log_{10}H_V$, which implies that the addition of V and C increases H_V. *From* Figure 3B*, it is evident that* $log_{10}\sigma$*,* $log_{10}\sigma_y$*, and* $log_{10}H_V$ *have a strong positive linear correlation with each other*. Therefore, $log_{10}H_V$ was utilized as the main mechanical property prediction and experimental validation in this study.

Thus, seven properties – M_s, $log_{10}H_c$, $log_{10}T_c$, $log_{10}\rho$, $log_{10}\delta$, $log_{10}H_V$, and $log_{10}Cost$ – were chosen as the responses for the multi-property ML model, as listed in Table 1. Before building the multi-property model, the experimental data available in the database for the responses was analyzed, as shown in Figure 3C. The *Cost* was calculated from the alloy composition; hence, the $log_{10}Cost$ column is 100% filled in the database. M_s and $log_{10}T_c$ have the most experimental data, i.e., 75% and 72% of the data entries, respectively. In the case of T_c, the data for the binary alloy compositions was obtained from the phase diagram, the data for commercial alloy compositions such as Hiperco was obtained from the reported sources.

$log_{10}H_V$ has the least experimental data, which is 14.5% of the total data entries, which shows that only a limited number of mechanical property studies have been performed on Fe-Co-Ni-based magnetic alloys. Figure 3C shows that only a small number of rows in the database are complete, i.e., 0.66% of the data entries, which corresponds to just 8 rows. Therefore, an ML-based imputation strategy was developed to fill the empty cells of the responses column to build a multi-property model, which is discussed in Section imputation strategy.

Imputation strategy

Figure 4 shows the heatmap of MAE, RMSE, and R^2 values of the all the regression models built to find the best model for the imputation of the property. The best regression models used for stepwise imputation are shown in Table 2 along with their MAE, RMSE, and R^2 values.

Forward design of the multi-property alloy

Multi-property models

Figure 5A–5C shows the heatmap of the performance metrics (MAE, RMSE, and R^2) of the six models with composition as the input features to the six models. Among them, the ETR model was found to be the best predictive model with the lowest MAE and high R^2 for all the properties. The ETR model can predict a novel composition within the limits of each property value in the database which achieves an optimum balance of properties.[43,127,128] The performance of the ETR model in predicting M_s, $log_{10}T_c$, and $log_{10}Cost$ is better and more accurate, the model exhibits $R^2 > 0.95$ and MAE <0.05. This can be attributed to the strong compositional dependence of M_s and T_c. As *Cost* is calculated using composition and individual element cost, it explains the good performance of the ETR model. The performance of the ETR model for predicting $log_{10}\delta$ is moderately good and accurate with a good R^2, in the range of 0.85–0.9, and low MAE. For $log_{10}H_c$, the performance of the ETR model is less accurate with good R^2, in the range of 0.85–0.9, and a high MAE. For $log_{10}\rho$ and $log_{10}H_V$, the performance of the ETR model is moderately accurate and precise with decent R^2, in the range of 0.75–0.8, and low MAE. H_c, ρ, and H_V are more process-dependent properties compared to composition, which explains this moderate performance of the ETR model.

Among the NN architectures, NNR_4layers performed the best with lowest MAE for all the properties and highest R^2 for M_s, $log_{10}\delta$, and $log_{10}Cost$. However, the model exhibited the second lowest R^2 values for $log_{10}H_c$, $log_{10}T_c$, and $log_{10}\rho$ and the second highest R^2 value for $log_{10}H_V$. Wen et al. designed a high entropy alloys with hardness higher than the training database by using 2 iterations of ML combined with experiments in which they implemented the ML model with only compositional input features in the first loop and the ML model with compositional and physical features in the second loop.[38] They reported that designing alloys with both compositions and physical features was more effective than designing alloys with only compositional features. Hence, WenAlloys featurizer class in Matminer[129] package was used to evaluate the physical features for all the data in the imputed database and built all six models with the same hyperparameters to

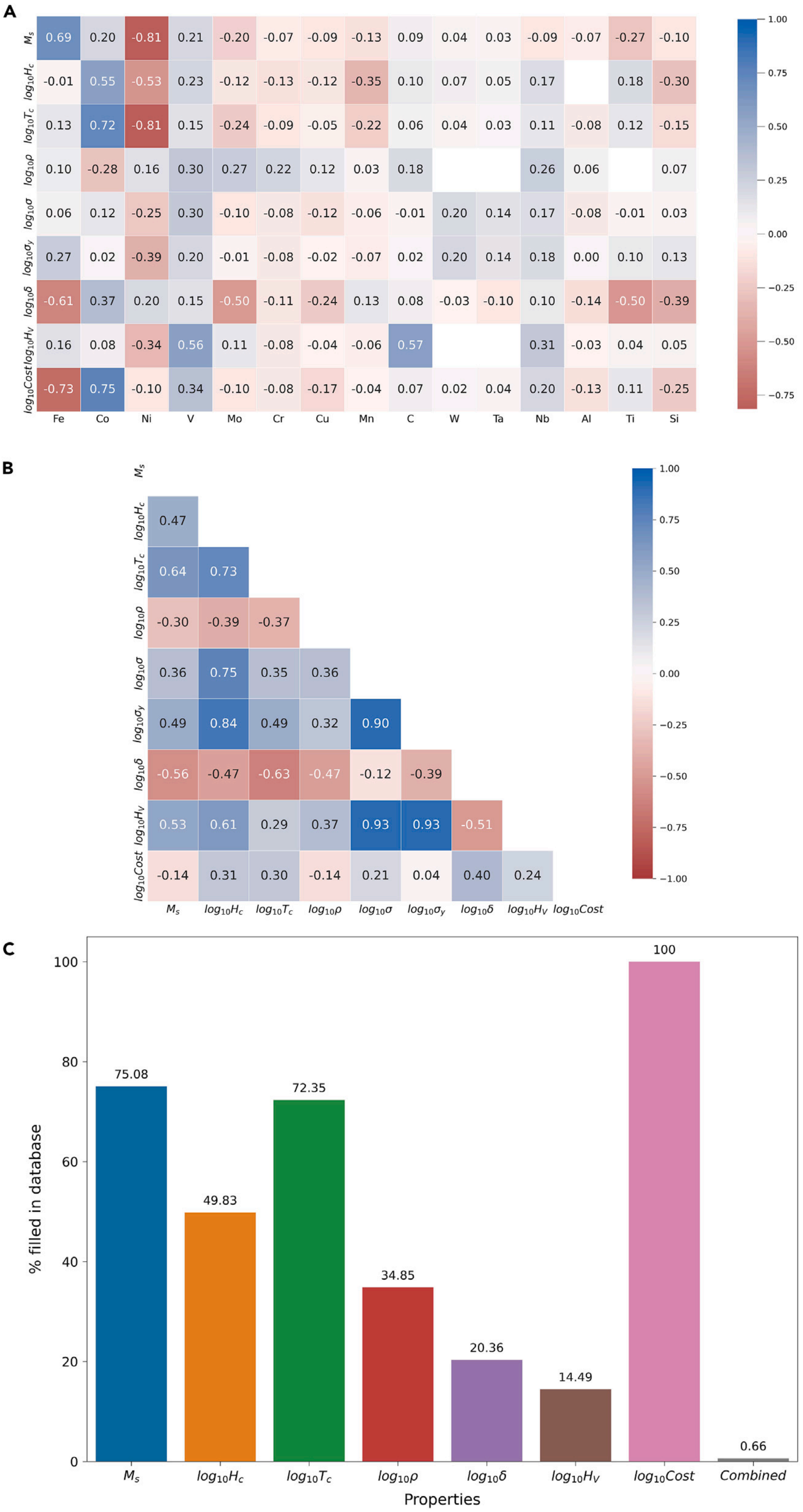

	Fe	Co	Ni	V	Mo	Cr	Cu	Mn	C	W	Ta	Nb	Al	Ti	Si
M_s	0.69	0.20	-0.81	0.21	-0.20	-0.07	-0.09	-0.13	0.09	0.04	0.03	-0.09	-0.07	-0.27	-0.10
$log_{10}H_c$	-0.01	0.55	-0.53	0.23	-0.12	-0.13	-0.12	-0.35	0.10	0.07	0.05	0.17		0.18	-0.30
$log_{10}T_c$	0.13	0.72	-0.81	0.15	-0.24	-0.09	-0.05	-0.22	0.06	0.04	0.03	0.11	-0.08	0.12	-0.15
$log_{10}\rho$	0.10	-0.28	0.16	0.30	0.27	0.22	0.12	0.03	0.18			0.26	0.06		0.07
$log_{10}\sigma$	0.06	0.12	-0.25	0.30	-0.10	-0.08	-0.12	-0.06	-0.01	0.20	0.14	0.17	-0.08	-0.01	0.03
$log_{10}\sigma_y$	0.27	0.02	-0.39	0.20	-0.01	-0.08	-0.02	-0.07	0.02	0.20	0.14	0.18	0.00	0.10	0.13
$log_{10}\delta$	-0.61	0.37	0.20	0.15	-0.50	-0.11	-0.24	0.13	0.08	-0.03	-0.10	0.10	-0.14	-0.50	-0.39
$log_{10}H_V$	0.16	0.08	-0.34	0.56	0.11	-0.08	-0.04	-0.06	0.57			0.31	-0.03	0.04	0.05
$log_{10}Cost$	-0.73	0.75	-0.10	0.34	-0.10	-0.08	-0.17	-0.04	0.07	0.02	0.04	0.20	-0.13	0.11	-0.25

	M_s	$log_{10}H_c$	$log_{10}T_c$	$log_{10}\rho$	$log_{10}\sigma$	$log_{10}\sigma_y$	$log_{10}\delta$	$log_{10}H_V$	$log_{10}Cost$
M_s									
$log_{10}H_c$	0.47								
$log_{10}T_c$	0.64	0.73							
$log_{10}\rho$	-0.30	-0.39	-0.37						
$log_{10}\sigma$	0.36	0.75	0.35	0.36					
$log_{10}\sigma_y$	0.49	0.84	0.49	0.32	0.90				
$log_{10}\delta$	-0.56	-0.47	-0.63	-0.47	-0.12	-0.39			
$log_{10}H_V$	0.53	0.61	0.29	0.37	0.93	0.93	-0.51		
$log_{10}Cost$	-0.14	0.31	0.30	-0.14	0.21	0.04	0.40	0.24	

Figure 3. Exploratory data analysis

Pearson correlation coefficients heatmap of (A) properties vs. elements and (B) properties vs. properties.
(C) Percentage of properties data available for the alloy compositions in the database.

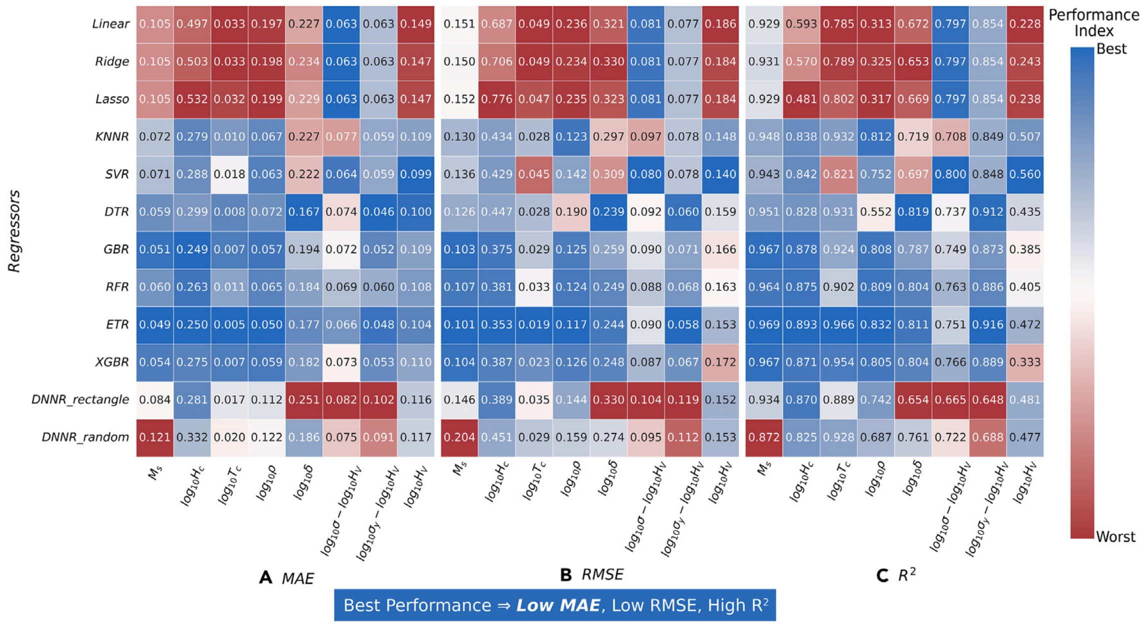

A MAE

Regressors	M_s	$log_{10}H_c$	$log_{10}T_c$	$log_{10}\rho$	$log_{10}\delta$	$log_{10}\sigma - log_{10}H_V$	$log_{10}\sigma_y - log_{10}H_V$	$log_{10}H_V$
Linear	0.105	0.497	0.033	0.197	0.227	0.063	0.063	0.149
Ridge	0.105	0.503	0.033	0.198	0.234	0.063	0.063	0.147
Lasso	0.105	0.532	0.032	0.199	0.229	0.063	0.063	0.147
KNNR	0.072	0.279	0.010	0.067	0.227	0.077	0.059	0.109
SVR	0.071	0.288	0.018	0.063	0.222	0.064	0.059	0.099
DTR	0.059	0.299	0.008	0.072	0.167	0.074	0.046	0.100
GBR	0.051	0.249	0.007	0.057	0.194	0.072	0.052	0.109
RFR	0.060	0.263	0.011	0.065	0.184	0.069	0.060	0.108
ETR	0.049	0.250	0.005	0.050	0.177	0.066	0.048	0.104
XGBR	0.054	0.275	0.007	0.059	0.182	0.073	0.053	0.110
DNNR_rectangle	0.084	0.281	0.017	0.112	0.251	0.082	0.102	0.116
DNNR_random	0.121	0.332	0.020	0.122	0.186	0.075	0.091	0.117

B RMSE

Regressors	M_s	$log_{10}H_c$	$log_{10}T_c$	$log_{10}\rho$	$log_{10}\delta$	$log_{10}\sigma - log_{10}H_V$	$log_{10}\sigma_y - log_{10}H_V$	$log_{10}H_V$
Linear	0.151	0.687	0.049	0.236	0.321	0.081	0.077	0.186
Ridge	0.150	0.706	0.049	0.234	0.330	0.081	0.077	0.184
Lasso	0.152	0.776	0.047	0.235	0.323	0.081	0.077	0.184
KNNR	0.130	0.434	0.028	0.123	0.297	0.097	0.078	0.148
SVR	0.136	0.429	0.045	0.142	0.309	0.080	0.078	0.140
DTR	0.126	0.447	0.028	0.190	0.239	0.092	0.060	0.159
GBR	0.103	0.375	0.029	0.125	0.259	0.090	0.071	0.166
RFR	0.107	0.381	0.033	0.124	0.249	0.088	0.068	0.163
ETR	0.101	0.353	0.019	0.117	0.244	0.090	0.058	0.153
XGBR	0.104	0.387	0.023	0.126	0.248	0.087	0.067	0.172
DNNR_rectangle	0.146	0.389	0.035	0.144	0.330	0.104	0.119	0.152
DNNR_random	0.204	0.451	0.029	0.159	0.274	0.095	0.112	0.153

C R^2

Regressors	M_s	$log_{10}H_c$	$log_{10}T_c$	$log_{10}\rho$	$log_{10}\delta$	$log_{10}\sigma - log_{10}H_V$	$log_{10}\sigma_y - log_{10}H_V$	$log_{10}H_V$
Linear	0.929	0.593	0.785	0.313	0.672	0.797	0.854	0.228
Ridge	0.931	0.570	0.789	0.325	0.653	0.797	0.854	0.243
Lasso	0.929	0.481	0.802	0.317	0.669	0.797	0.854	0.238
KNNR	0.948	0.838	0.932	0.812	0.719	0.708	0.849	0.507
SVR	0.943	0.842	0.821	0.752	0.697	0.800	0.848	0.560
DTR	0.951	0.828	0.931	0.552	0.819	0.737	0.912	0.435
GBR	0.967	0.878	0.924	0.808	0.787	0.749	0.873	0.385
RFR	0.964	0.875	0.902	0.809	0.804	0.763	0.886	0.405
ETR	0.969	0.893	0.966	0.832	0.811	0.751	0.916	0.472
XGBR	0.967	0.871	0.954	0.805	0.804	0.766	0.889	0.333
DNNR_rectangle	0.934	0.870	0.889	0.742	0.654	0.665	0.648	0.481
DNNR_random	0.872	0.825	0.928	0.687	0.761	0.722	0.688	0.477

Figure 4. Heatmap of performance metrics

(A) mean absolute error (MAE), (B) root mean squared error (RMSE), and (C) coefficient of determination (R^2) of various ML regressor models for the imputation of each property. The lowest MAE model is chosen for the imputation of each property which is indicated with the darkest shade of blue in (A) for each column.

compare their performance with the models with only compositional features as input. Figures 5D–5F shows the heatmap of the performance metrics (MAE, RMSE, and R^2) of the six models with composition and physical descriptors as the input features for the six models.

It can be observed that the performance of tree-based models does not change with the addition of physical features as input, as shown in the bar plots in Figures 5G–5I. However, the performance of the NN models is improved after the addition of physical features as input, especially for NNR_4layers. The comparison of the performance of NNR_4layers and NNR_4layers_Wen (NNR_4layers with composition and Wen alloy features as input) is shown in the bar plots in Figures 5G–5I. The predicted vs. experimental values plots along with their performance metrics of each property for these 4 models are presented in Section S3 of supplementary information. The NNR_4layers_Wen model performed better in predicting properties compared to other NN architecture models but not better than the ETR model. Thus, the ETR and NNR_4layers_Wen models were selected for experimental validation.

Experimental validation

The predictions of the multi-property ETR and NNR_4layers_Wen models were compared with the experimental values of the properties as shown in Figure 6. In Figure 6A, for 0.9 T < M_s < 1.4 T, both the models predicted values within ±10% range of the experimental values. For M_s > 1.4 T, both the models overpredicted compared to the experimental values and approximately 55% of the predictions by ETR and 72.5% of the predictions by NNR_4layers_Wen have more than 10% error from experimental values. The overprediction by the models could be due to the fact that the high M_s alloys in the database are mainly binary FeCo alloys or FeCo alloys with the addition of V, while the predictions performed were for ternary Fe-Co-Ni alloys. In Figure 6B, it can be observed that the models underpredicted the $log_{10}H_c$ values which can be

Table 2. Best ML regressor model used for the imputation of each property

Step No.	Mapping	Best ML Regressor for imputation (MAE, RMSE, R^2)
1	Composition to M_s	Extra Trees (0.049, 0.101, 0.97)
2	Composition to $log_{10}H_c$	Extra Trees (0.249, 0.353, 0.89)
3	Composition to $log_{10}T_c$	Extra Trees (0.006, 0.02, 0.97)
4	Composition to $log_{10}\,\rho$	Extra Trees (0.05, 0.117, 0.83)
5	Composition to $log_{10}\,\delta$	Decision Tree (0.167, 0.239, 0.82)
6	$log_{10}\,\sigma$ to $log_{10}H_V$	Linear (0.063, 0.081, 0.8)
7	$log_{10}\,\sigma_y$ to $log_{10}H_V$	Decision Tree (0.06, 0.047, 0.91)
8	Composition to $log_{10}H_V$	Support Vector (0.14, 0.099, 0.56)

Table 3. Selected properties of commonly used commercial magnetic alloys

Alloy	M_s (T)	H_c (A/m)	T_c (K)	ρ ($\mu\Omega\cdot$cm)	H_V (HV)	Calculated *Cost* ($/kg)	Reference
$Fe_{94.21}Si_{5.79}$	2.03	6.4	1018	45–48	170–195	0.46	Moses [130,131]
$Fe_{87.86}Si_{12.14}$	1.8	–	973	82	395	0.51	Kasai and Abe et al. [132,133]
$Fe_{49}Co_{49}V_2$	2.4	16–398	1203	27	180–220	23.35	Gutfleisch Fiorillo and Tan et al.[2,134,135]
Fe	2.16	4–80	1044	10	150	0.42	Gutfleisch et al. [2,64]
$Fe_{50}Ni_{50}$	1.4–1.6	4–20	753	40–50	120–180	7.33	Gutfleisch Fiorillo, Tan et al [2,134–136]
$Ni_{78}Fe_{17}Mo_5$	0.65–0.82	0.25–0.64	673	60	160	13.86	Gutfleisch et al. and ASTM International [2,137]
$Fe_{53}Ni_{30}Co_{17}$	1.2	63.66–71.62	703	43	160–230	10.24	Special Metals The NILO® and NILOMAG® Nickel-Iron Alloys[138]

due to the high bias in the curated database a containing higher number of reported H_c values for sheets and ingot samples prepared by the casting method and the experimental procedure used for validation by powder metallurgy techniques. Similarly, the models underpredicted $log_{10}\,\rho$ values too as shown in Figure 6D. Moreover, H_c and ρ depend on the processing conditions of the alloys which influence the structure of the alloys, which is not considered in both the models.

For $log_{10}T_c$ and $log_{10}H_V$, it can be observed in Figures 6C and 6E, the ETR model predicted all the values within ±10% range of the experimental values. However, the NNR_4layers_Wen model predicted 100% of $log_{10}T_c$ and 97.5% of $log_{10}H_V$ values. The predictions for $log_{10}T_c$ by both the models matched well the experimental values. For $log_{10}H_V$, both the models overpredicted compared to experimental values which can be attributed to the bias in the database containing a higher number of reported H_V values for sintered binary alloys with the addition of other elements and few reported H_V values for ternary alloys in the form of sheets. Finally, for $log_{10}Cost$, both the models predicted 97.5% values within the ±10% range of the experimental values. As shown in Figure 6F, for $log_{10}Cost < 0.95$, the ETR model underpredicted and the NNR_4layers_Wen model overpredicted. As expected, for $log_{10}Cost < 0.95$, both the models made accurate predictions. The experimental values and the predicted values for all the 40 compositions and calculated MAE of each property for both the models are tabulated in Section S4 *of the* supplementary information.

This shows that for a given Fe-Co-Ni alloy composition, both ETR and NNR_4layers_Wen model would predict the $log_{10}T_c$ and $log_{10}Cost$ with high accuracy and the $log_{10}H_V$ and M_s with moderate accuracy. Overall, the performance of both models deployed on the experimental data are comparable to each other with NNR_4layers_Wen performing better than the ETR model. However, on the main database, the performance of the ETR model was better than that of NNR_4layers_Wen model. Thus, both the models were considered for designing multi-property alloys using Bayesian optimization.

Inverse design of the multi-property alloy

Multi-objective Bayesian optimization

For designing alloy compositions using the ETR model, the objective function defined in Equations 1, 2, 3, and 4 is used in BO. For using the NNR_4layers_Wen model, the objective function is modified to include the Wen alloy features between Equations 4 and 6 and is described by the equations later in discussion,

$$add_{feat} = WenAlloys.featurize\left(Composition\left(x_n\right)\right) \quad \text{(Equation 5)}$$

$$x_{all} = concatenate\left(x_n, add_{feat}\right) \quad \text{(Equation 6)}$$

$$x_{transformed} = StandardScaler\left(x_{all}\right) \quad \text{(Equation 7)}$$

where add_{feat} in Equation 5 is the Wen alloy features array calculated using WenAlloys featurizer in matminer, x_n in Equations 5 and 6 is the normalized compositional array, *StandardScaler* in Equation 7 is the standard scaling function used on the train set for building multi-property NNR_4layers_Wen model.

For the acquisition function "EI" (as mentioned in Section multi-objective bayesian optimization for inverse design of the multi-property alloy), the *xi* parameter value in gp_minimize was assigned the default value of 0.01. The *xi* parameter controls how much the acquisition value favors exploration and exploitation. For the mentioned set value, the acquisition function will favor more exploitation and less exploration. This means the algorithm will search for a promising region in the search and probe to improve a promising solution. For the case of searching ternary Fe-Co-Ni alloy composition, this is beneficial as the search space is not as vast as a high entropy alloy or complex multi-component alloy.

The properties used in the objective function of MOBO (described in Equation 7) to design Fe-Co-Ni alloy compositions are M_s, T_c, and *Cost* because M_s and T_c are composition-dependent properties. *Cost* is calculated using the composition and individual element price which

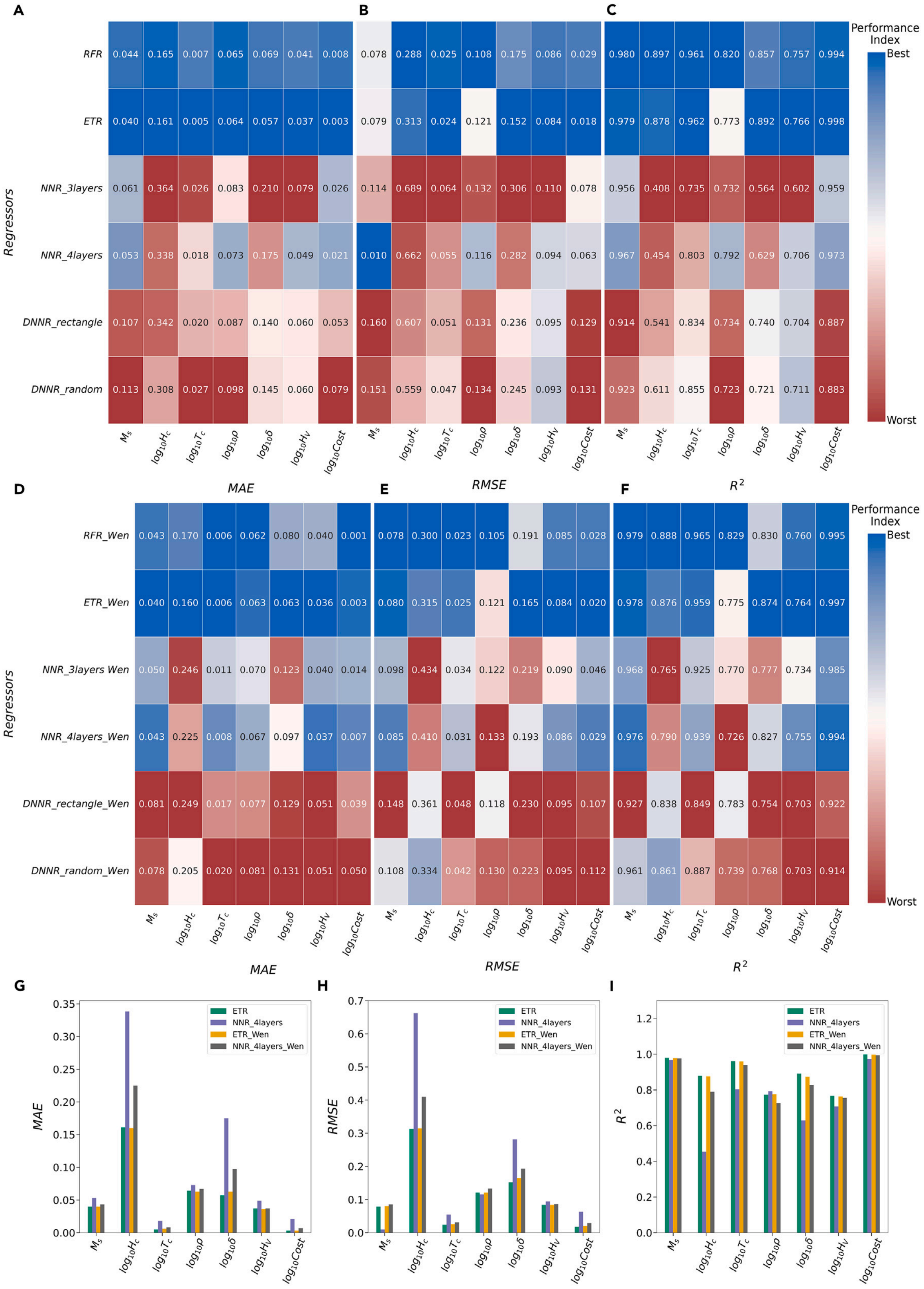

A

Regressors	M_S	$log_{10}H_c$	$log_{10}T_c$	$log_{10}\rho$	$log_{10}\delta$	$log_{10}H_V$	$log_{10}Cost$
RFR	0.044	0.165	0.007	0.065	0.069	0.041	0.008
ETR	0.040	0.161	0.005	0.064	0.057	0.037	0.003
NNR_3layers	0.061	0.364	0.026	0.083	0.210	0.079	0.026
NNR_4layers	0.053	0.338	0.018	0.073	0.175	0.049	0.021
DNNR_rectangle	0.107	0.342	0.020	0.087	0.140	0.060	0.053
DNNR_random	0.113	0.308	0.027	0.098	0.145	0.060	0.079

B

Regressors	M_S	$log_{10}H_c$	$log_{10}T_c$	$log_{10}\rho$	$log_{10}\delta$	$log_{10}H_V$	$log_{10}Cost$
RFR	0.078	0.288	0.025	0.108	0.175	0.086	0.029
ETR	0.079	0.313	0.024	0.121	0.152	0.084	0.018
NNR_3layers	0.114	0.689	0.064	0.132	0.306	0.110	0.078
NNR_4layers	0.010	0.662	0.055	0.116	0.282	0.094	0.063
DNNR_rectangle	0.160	0.607	0.051	0.131	0.236	0.095	0.129
DNNR_random	0.151	0.559	0.047	0.134	0.245	0.093	0.131

C

Regressors	M_S	$log_{10}H_c$	$log_{10}T_c$	$log_{10}\rho$	$log_{10}\delta$	$log_{10}H_V$	$log_{10}Cost$
RFR	0.980	0.897	0.961	0.820	0.857	0.757	0.994
ETR	0.979	0.878	0.962	0.773	0.892	0.766	0.998
NNR_3layers	0.956	0.408	0.735	0.732	0.564	0.602	0.959
NNR_4layers	0.967	0.454	0.803	0.792	0.629	0.706	0.973
DNNR_rectangle	0.914	0.541	0.834	0.734	0.740	0.704	0.887
DNNR_random	0.923	0.611	0.855	0.723	0.721	0.711	0.883

D MAE

Regressors	M_S	$log_{10}H_c$	$log_{10}T_c$	$log_{10}\rho$	$log_{10}\delta$	$log_{10}H_V$	$log_{10}Cost$
RFR_Wen	0.043	0.170	0.006	0.062	0.080	0.040	0.001
ETR_Wen	0.040	0.160	0.006	0.063	0.063	0.036	0.003
NNR_3layers Wen	0.050	0.246	0.011	0.070	0.123	0.040	0.014
NNR_4layers_Wen	0.043	0.225	0.008	0.067	0.097	0.037	0.007
DNNR_rectangle_Wen	0.081	0.249	0.017	0.077	0.129	0.051	0.039
DNNR_random_Wen	0.078	0.205	0.020	0.081	0.131	0.051	0.050

E RMSE

Regressors	M_S	$log_{10}H_c$	$log_{10}T_c$	$log_{10}\rho$	$log_{10}\delta$	$log_{10}H_V$	$log_{10}Cost$
RFR_Wen	0.078	0.300	0.023	0.105	0.191	0.085	0.028
ETR_Wen	0.080	0.315	0.025	0.121	0.165	0.084	0.020
NNR_3layers Wen	0.098	0.434	0.034	0.122	0.219	0.090	0.046
NNR_4layers_Wen	0.085	0.410	0.031	0.133	0.193	0.086	0.029
DNNR_rectangle_Wen	0.148	0.361	0.048	0.118	0.230	0.095	0.107
DNNR_random_Wen	0.108	0.334	0.042	0.130	0.223	0.095	0.112

F R^2

Regressors	M_S	$log_{10}H_c$	$log_{10}T_c$	$log_{10}\rho$	$log_{10}\delta$	$log_{10}H_V$	$log_{10}Cost$
RFR_Wen	0.979	0.888	0.965	0.829	0.830	0.760	0.995
ETR_Wen	0.978	0.876	0.959	0.775	0.874	0.764	0.997
NNR_3layers Wen	0.968	0.765	0.925	0.770	0.777	0.734	0.985
NNR_4layers_Wen	0.976	0.790	0.939	0.726	0.827	0.755	0.994
DNNR_rectangle_Wen	0.927	0.838	0.849	0.783	0.754	0.703	0.922
DNNR_random_Wen	0.961	0.861	0.887	0.739	0.768	0.703	0.914

Figure 5. Performance of multi-property regression models

(A) mean absolute error (MAE), (B) root mean squared error (RMSE), and (C) coefficient of determination (R^2) of various multi-property regressor (MPR) models with composition as model features.

(D) MAE, (E) RMSE, and (F) R^2 of the MPR models with composition and Wen alloy features as model features.

(G) MAE, (H) RMSE, (I) R^2 of extra trees regressor and neural network regression consisting of 4 hidden layers with and without Wen alloy features as model features.

makes it a composition-dependent property too. Moreover, in Section forward design of the multi-property alloy, it was observed that both the models are quite accurate in predicting these three properties compared to the predictions of other properties. The weights for optimizing these three properties are each set to 1 so that equal emphasis is given while designing the alloy composition. Thus, Equation 7 can be rewritten as the equation later in discussion.

$$objective = abs\left(target_{M_s} - pred_{M_s}\right) + abs\left(target_{T_c} - pred_{T_c}\right) + abs\left(target_{Cost} - pred_{Cost}\right) \quad \text{(Equation 11)}$$

To set the target values of M_s, T_c, and *Cost* for the inverse design of alloys, a survey of the target properties of the most commonly used alloys for various rotating electrical machines applications was conducted and is tabulated in Table 3. Based on the values of M_s, T_c, and *Cost* in the table, target values of M_s, T_c, and *Cost* were determined to be set in the range of 1.5–2.4 T, 970–1200 K, and 10\$–19\$/kg for discovering Fe-Co-Ni alloy compositions with a moderate to high M_s, high T_c, and low *Cost* (*Cost* values based on the individual elemental cost of Fe, Co, and Ni).

The set target values of M_s, T_c, and *Cost* for the inverse design are as follows:

1. BO Set 1: M_s – 1.5 T, T_c – 970 K, and *Cost* – 15 \$/kg.
2. BO Set 2: M_s – 1.75 T, T_c – 1000 K, and *Cost* – 11.5 \$/kg.
3. BO Set 3: M_s – 1.75 T, T_c – 1143 K, and *Cost* – 19 \$/kg.
4. BO Set 4: M_s – 2 T, T_c – 1070 K, and *Cost* – 10.5 \$/kg.
5. BO Set 5: M_s – 2.2 T, T_c – 1173 K, and *Cost* – 10 \$/kg.
6. BO Set 6: M_s – 2.4 T, T_c – 1173 K, and *Cost* – 10 \$/kg.

For each of the six sets of target values, our Bayesian optimization strategy was used to predict alloy compositions by performing 200 iterations of the acquisition function and among them 5 alloy compositions with the lowest acquisition function values were selected for experimental validation. For instance, the evolution of acquisition function value for ETR model is shown in Section S5 of the supplementary information.

Experimental validation

The predicted Fe-Co-Ni alloy compositions from Bayesian optimization and their respective predicted properties from ETR and NNR_4layers_Wen models are shown in Figure 7. These predicted alloy compositions were compared to the 40 rapidly synthesized Fe-Co-Ni compositions and their properties as shown in the ternary contour plots of M_s, T_c, H_c, ρ, H_V and *Cost*.

Comparing the composition predictions of target sets BO set 1 and BO set 2 for both models, it can be observed that Ni content decreased in the predicted composition with an increase in the set values of M_s and T_c. The Fe content increased with a decrease in the set value of the *Cost*, as shown in Figures 7A–7C. In the composition predictions for BO set 2 for both models, the Fe content was significantly high compared to the BO set 1 as the set values of M_s and *Cost* were higher and lower, respectively, as shown in Figures 7A and 7C.

For the BO set 1, the composition predictions for both models were similar to each other, and all the 5 predicted compositions were quite close to each other for both models, as shown in Figure 7. The predicted compositions for BO set 1 for the ETR model exhibited M_s values in the range of 1.54–1.58 T, T_c in the range of 900–912 K, and *Cost* in the range of 10.6\$–11.3\$/kg according to the experimental contour plots. Similarly, the predicted compositions for BO set 1 for the ETR model exhibited M_s in the range of 1.54–1.58 T, T_c in the range of 900–912 K, and *Cost* in the range of 11.4\$–11.7\$/kg, according to the experimental contour plots. The predicted compositions for BO set 1 for the NNR_4layers_Wen model consisted of higher Ni content compared to that for ETR model. The predicted compositions for BO set 2 for both the models exhibited M_s values in the range of 1.46–1.5 T, T_c in the range of 1000–1010 K, and *Cost* in the range of 15\$–15.5\$/kg, according to the experimental contour plots.

Comparing the composition predictions of target sets for BO set 2 and BO set 3 for both models, the Co content increased significantly in the predicted composition with an increase in set values of T_c and *Cost*, as shown in Figures 7B and 7C. Moreover, it can be observed that, for both models, the predicted compositions for BO set 3 consisted of a higher content of Co and a lower content of Ni when compared to that of BO set 1 due to the increase in set value of T_c and M_s, as shown in Figures 7A and 7B. The predicted compositions for BO set 3 for the ETR model exhibited M_s values in the range of 1.58–1.6 T, T_c in the range of 1090–1110 K, and *Cost* in the range of 18.5\$–19\$/kg, according to the experimental contour plots. Similarly, the predicted compositions for BO set 3 for the NNR_4layers_Wen model exhibited M_s in the range of 1.73–1.76 T, T_c in the range of 1100–1160 K, and *Cost* in the range of 18.5\$–20\$/kg, according to the experimental contour plots. The predicted compositions for BO set 3 for the NNR_4layers_Wen model consisted of higher Fe and Co content and lower Ni content compared to that for ETR model. The predicted composition with the lowest objective value for BO set 3 for the NNR_4layers_Wen model exhibited M_s in the range of 1.74 T, T_c of 1148 K, and *Cost* of 19.5 \$/kg according to the experimental contour plots.

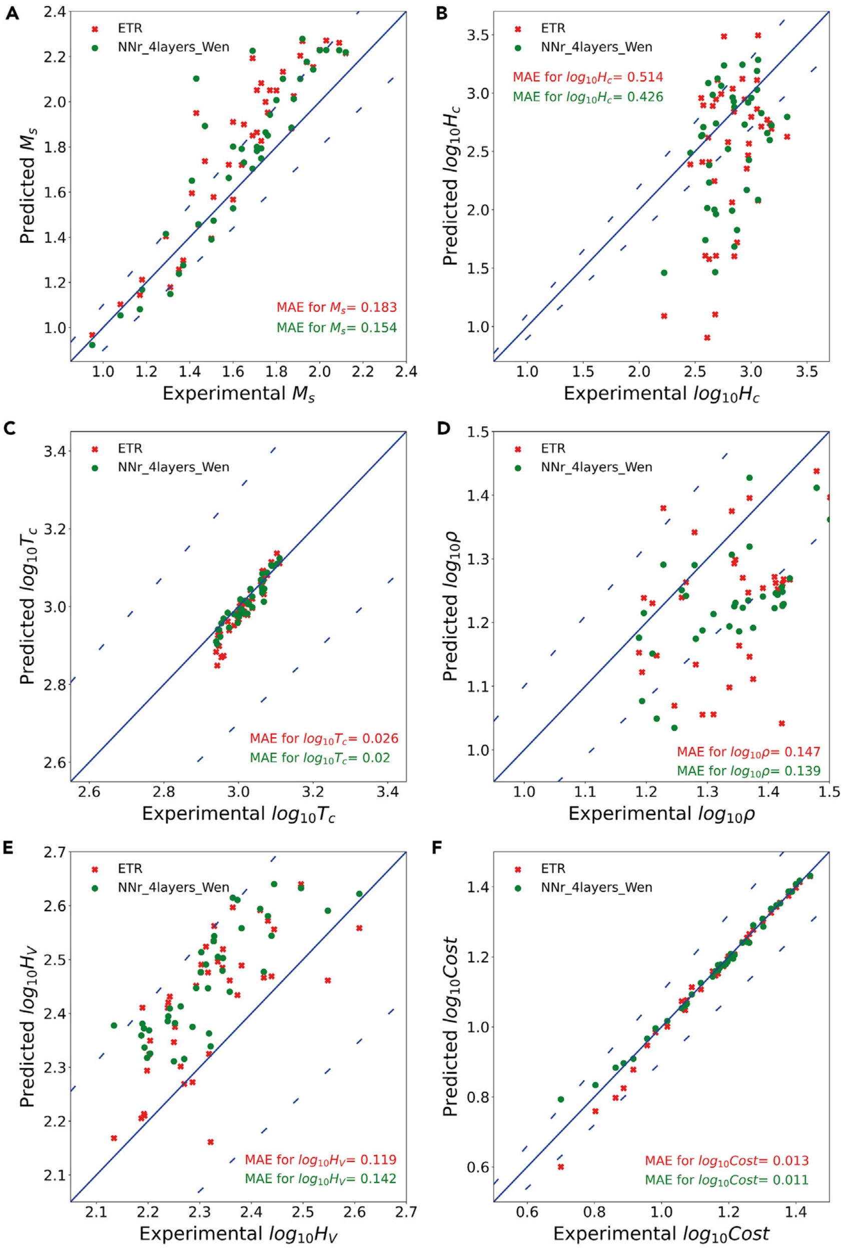

Figure 6. Experimental validation of selected multi-property models

Plot of experimental values vs. predicted values of (A) M_s, (B) $log_{10}H_c$, (C) $log_{10}T_c$, (D) $log_{10}\rho$, (E) $log_{10}H_V$, and (F) $log_{10}Cost$ with the ±10% error lines (dashed) for extra trees regressor with composition as input features (green) and neural network regressor with composition and Wen alloy features as input features (red).

The predicted compositions for BO sets 4, 5, and 6 for ETR model consisted of higher Fe and lower Ni content compared to that for BO sets 1, 2, and 3 as the set target value of M_s is higher and *Cost* is lower as shown in Figure 7. For the NNR_4layers_Wen model, the same trend was exhibited by BO sets 5 and 6 but the predicted compositions for BO set 4 consisted of higher Fe and Ni content compared to that for BO set 3, as shown in Figure 7. Further, it can be observed that in the predicted compositions for BO sets 4, 5, and 6 for both models, Fe content increased, and Ni content decreased with an increase in the set target values of M_s; Co content was higher for an increase in the set target values of T_c. These trends correlate well with the trends expected with domain expertise and the subset of these properties with Fe, Co, and Ni observed in the database, as explained in Section database curation and analysis. Also, it can be observed that the predicted compositions for BO sets 4, 5, and 6 for the NNR_4layers_Wen model were spread out over a wide range of compositions compared to that for the ETR model. This can be attributed to the multi-numbered and multi-level decision-based nature of the ETR model which would make the BO approach for

Table 4. Predicted compositions by MOBO for the six target sets and their respective experimental properties for BO sets 1 to 5 and predicted properties for BO set 6 using ETR model

BO Set No.	Alloy Composition	M_s (T)	H_c (A/m)	T_c (K)	ρ (μΩ·cm)	H_V (HV)	*Cost* ($/kg)
1	$Fe_{27.3}Co_{25}Ni_{47.7}$	1.47	385	1002	22.8	198	15.28
2	$Fe_{44.7}Co_{15.4}Ni_{39.9}$	1.58	570	890	40.3	210	11.1
3	$Fe_{23.5}Co_{40.8}Ni_{35.7}$	1.6	290	1103.7	31.5	188	18.75
4	$Fe_{50}Co_{20.8}Ni_{29.2}$	1.77	770	1002	30	248	11.48
5	$Fe_{61.9}Co_{22.8}Ni_{15.3}$	2.01	1350	1056.8	24.5	365	10.2
6	$Fe_{66.8}Co_{28}Ni_{5.2}$	2.38	362.1	1190.2	17.3	254.2	10.5

the compositions closer to each other. However, the complex non-linear inter-connected nature of the NNR_4layers_Wen model would give BO freedom to approach different compositions, some of which may be the local optimum points.

In Figures 7A–7C, it can be observed that the predicted compositions for BO set 4 exhibited lower M_s values according to the experimental contour plot compared to the set target value. However, for BO set 5, the predicted compositions exhibited similar M_s values according to the experimental contour plot compared to the set target value. The predicted compositions for BO set 4 for the ETR model exhibited M_s in the range of 1.73–1.78 T, T_c in the range of 990–1010 K, and *Cost* in the range of 10.8$–11.8$/kg, similar to the experimental contour plots. The predicted compositions for the BO set 5 for the ETR model exhibited M_s in the range of 1.98–2 T, T_c in the range of 1040–1065 K, and *Cost* in the range of 9.8$–10.4$/kg, according to the experimental contour plots. The predicted composition with the lowest objective value for the BO set 4 for the NNR_4layers_Wen model exhibited a M_s of 1.79T, T_c of 1020 K, and *Cost* of 12.7 $/kg, similar to the experimental contour plots. The predicted composition with the lowest objective value for BO set 5 for the NNR_4layers_Wen model was almost overlapping with the existing experimental composition of $Fe_{61.3}Co_{19.3}Ni_{19.4}$, which exhibited a M_s of 1.94 T, T_c of 1000 K, and *Cost* of 9.6 $/kg.

For the predicted compositions for all the BO sets for ETR model, the color of the predicted H_c values was blue according to the experimental contour plot color bar, as shown in Figure 7D. The range of predicted H_c values for the predicted compositions using the ETR model was as follows: BO set 1 in the range of 3–4.2 A/m, BO set 2 in the range of 38–45 A/m, BO set 3 in the range of 353–369 A/m, BO set 4 in the range of 311–333.5 A/m, BO set 5 in the range of 549–569 A/m, and BO set 6 in the range of 362–434 A/m. Considering the experimental contour lines, the predictions for BO set 3 using the ETR model were closest to experimental values.

The range of predicted H_c values for the predicted compositions using the NNR_4layers_Wen model was as follows: BO set 1 in the range of 109–122 A/m, BO set 2 in the range of 55–60 A/m, BO set 3 in the range of 805–964 A/m, BO set 4 in the range of 97–379 A/m, BO set 5 in the range of 506–1306 A/m, and BO set 6 in the range of 894–1146 A/m. Considering the experimental contour lines, the predictions for H_c for the predicted compositions using the NNR_4layers_Wen model were not close to the experimental values.

For ρ, the predicted values for the predicted compositions for BO sets 1–5 using the ETR model were in the range of 18–24 μΩ cm, which implies that it is challenging to discover Fe-Co-Ni compositions having ρ greater than 30 μΩ cm using the ETR model. The prediction of ρ for all BO sets compositions were also lower than the estimated actual values from the contour plot in Figure 7E. For the BO set 6, the predicted ρ for the predicted compositions was in the range 16–17.3 μΩ cm, which can be close to the actual value.

Similarly, the predicted ρ values for predicted compositions for BO sets 1–5 using the NNR_4layers_Wen model were in the range of 14–23 μΩ cm, which implies that it is challenging to discover Fe-Co-Ni compositions having ρ greater than 30 μΩ cm using the NNR_4layers_Wen model. The ρ values in the database would be in this range and most of the samples are prepared starting from the casting method which is a different method of synthesis compared to the experimental validation method.

For H_V, it can be observed from Figure 7F that the predicted values for the predicted compositions of all the BO sets using the ETR model were closer to the experimental values than those using the NNR_4layers_Wen model by comparing the color trend of the contour lines.

To analyze further the performance of the inverse design strategy using both MPR models, the predicted composition with the lowest objective value for the BO sets 1–5 for both models was considered. The predicted properties were compared to the experimental values obtained from the contour plots to calculate the deviation percentages. These results are tabulated in Section S5 *of the* supplementary information. The composition predicted for BO set 1 for the ETR model has a 2% lower experimental M_s value and for BO sets 2–5 have 8.5–11.5% lower experimental M_s values compared to the predicted M_s values. Similarly, the composition predicted for BO set 1 for the NNR_4layers_Wen model has a 2% lower experimental M_s value, for BO set 3, it has a 1.1% lower experimental M_s value and for BO sets 2, 4, and 5, it has 11% lower experimental values compared to predicted M_s values.

The composition predicted for BO sets 1–3 for the ETR model have 4–7% higher experimental T_c values, for BO set 4 has 14.8% higher experimental T_c value, and for BO set 5 has just 0.9% higher experimental T_c value compared to the predicted T_c values. The composition predicted for BO sets 1–5 for the NNR_4layers_Wen model have 5–9% higher experimental T_c values compared to the predicted T_c values.

For *Cost*, the composition predicted for the BO sets 1–5 for both models has predicted values quite similar to experimental values. This is because *Cost* is calculated using the weighted average of elemental costs.

The average deviation of the predicted M_s, T_c, and *Cost* values of the predicted compositions were 8.2% higher, 6.4% lower, and 1.1% lower compared to the experimental values, respectively, for the ETR model. The average deviation of predicted M_s, T_c, and *Cost* values

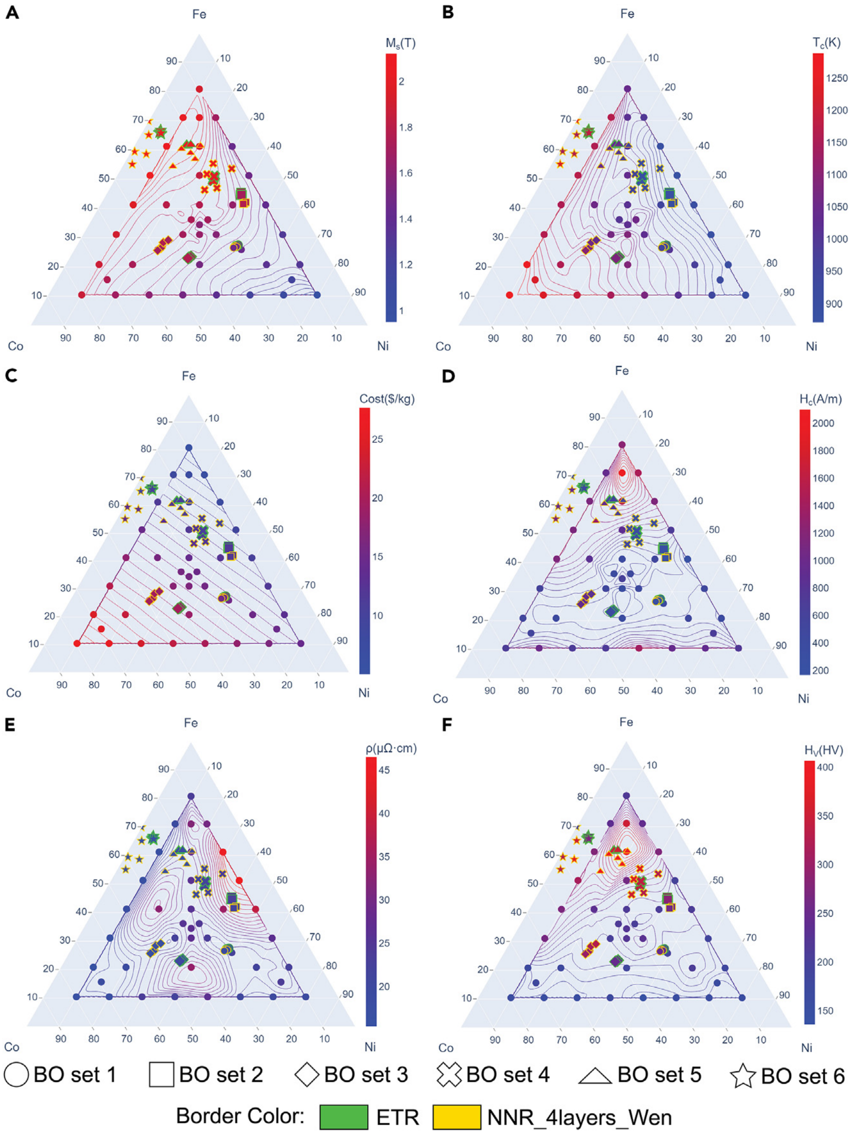

Figure 7. Experimental validation of inverse design strategy

Ternary contour plot of (A) M_s, (B) $log_{10}T_c$, (C) $log_{10}Cost$, (D) $log_{10}H_c$, (E) $log_{10}\rho$, and (F) $log_{10}H_V$ of 40 experimentally synthesized Fe-Co-Ni alloy compositions with predicted compositions from inverse design strategy with their respective predicted property values from ETR (points with green border) and NNR_4layers_Wen (points with yellow border) for 6 target sets.

of the predicted compositions were 7.2% higher, 6.6% lower, and 0.4% lower compared to the experimental values, respectively, for the ETR model.

The deviations of the predicted H_c values of the predicted compositions for the BO sets 1–5 for both models were quite high compared to the experimental H_c values. This could be attributed to the well-known dependence of H_c on processing parameters, microstructure, and heat treatment parameters. Similarly, the average deviations of predicted ρ values of the predicted compositions for the BO sets 1–5 for both models were 45–46% higher compared to the experimental ρ values. Finally, the predicted H_V values of the predicted compositions for the BO sets 1 and 5 for the ETR model were very close to the experimental H_V values, with a deviation of 1.8% and 5.2%, respectively. The predicted H_V values of the predicted compositions for the BO sets 2, 3, and 4 for the ETR model were 20–29% higher compared to the experimental H_V values. The average deviation of the predicted H_V values of the predicted compositions for the ETR model was 14.2% higher compared to the experimental H_V values. On the other hand, the predicted H_V values of the predicted compositions for the NNR_4layers_Wen model exhibited higher deviation percentages compared to that for the ETR model except for BO set 5. Overall, the average deviation of predicted H_V values of the predicted compositions for the NNR_4layers_Wen model was 22.9% higher compared to the experimental H_V values.

It can be inferred that the BO composition predictions and their predicted property values using the ETR model performed slightly better compared to that from the NNR_4layers_Wen model with a similar prediction performance for M_s, T_c, and *Cost* and better prediction performance for H_V. The predicted composition with the lowest objective value of MOBO for each target set using the ETR model and their respective approximate experimental properties for BO sets 1 to 5 and predicted properties for BO set 6 are tabulated in Table 4. Comparing the predicted property values of the BO predicted compositions for the ETR model, $Fe_{66.8}Co_{28}Ni_{5.2}$ (predicted M_s – 2.38 T, T_c – 1190.2 K, H_c – 362.1 A/m, ρ – 17.3 $\mu\Omega$ cm, H_V – 254.2 HV and *Cost* – 10.5$/kg) and $Fe_{61.9}Co_{22.8}Ni_{15.3}$ (predicted M_s – 2.22 T, T_c – 1047.5 K, H_c – 549.5 A/m, ρ – 18.7 $\mu\Omega$ cm, H_V – 347.1 HV and *Cost* – 10$/kg) demonstrate superior multi-property performance compared to previous reports, and performance comparable to recently designed Fe-Co-Ni alloys using accelerated experimental methodology.[123,135]

Conclusion and outlook

We curated a database of bulk Fe-Co-Ni-based magnetic alloys containing magnetic, mechanical, and electrical properties. The database is heterogeneous as alloys synthesized using different methods are included. The gaps in the database were filled using a unique ML-based multi-step imputation strategy. A comparative study of the performance of 12 different ML regression models, from linear regression models to various tree-based models to DNNs, mapping from composition to each property and mapping between mechanical properties was performed. The best model with the lowest MAE was chosen to fill the empty spaces for that property column. This imputed database was used to develop a multi-property model (forward design) mapping from composition to all the properties by using 6 different models. Apart from using only compositional input features, physical descriptors (Wen alloy features) were also used as input features to develop multi-property models using these 6 models. The best model with the lowest MAE, i.e., the ETR model, and the best neural network model with lowest MAE, i.e., NNR_4layers_Wen was chosen.

Further, a multi-objective BO (inverse design) was developed to predict alloy compositions by providing a target set of properties. Both the forward and inverse design methodology were experimentally validated by using 40 Fe-Co-Ni alloy compositions synthesized and characterized using high-throughput techniques. Overall, the ETR model performed better compared to the NNR_4layers_Wen model in both forward and inverse design strategies. Finally, two alloy compositions $Fe_{65.84}Co_{28.66}Ni_{5.5}$ and $Fe_{61.5}Co_{23.14}Ni_{15.35}$ were obtained from inverse design using ETR model with the optimum combination of $M_s > 2$ T, $T_c > 1050$K, $H_V > 250$ HV, $H_c < 1400$ A/m, $\rho > 17$ $\mu\Omega$ cm, and *Cost* $\approx$ 10 $/kg. The predicted properties value of the predicted compositions by MOBO were within 14% of the experimental values for M_s, T_c, *Cost*, and H_V. Our proposed approach can be used to design any class of materials using a heterogeneous database.

STAR★METHODS

Detailed methods are provided in the online version of this paper and include the following:

- KEY RESOURCES TABLE
- RESOURCE AVAILABILITY
  - Lead contact
  - Materials availability
  - Data and code availability
- EXPERIMENTAL MODEL AND STUDY PARTICIPANT DETAILS
- METHOD DETAILS
- QUANTIFICATION AND STATISTICAL ANALYSIS

SUPPLEMENTAL INFORMATION

Supplemental information can be found online at https://doi.org/10.1016/j.isci.2024.109723.

ACKNOWLEDGMENTS

This work is supported by the AME Programmatic Fund by the Agency for Science, Technology and Research, Singapore under Grant No. A1898b0043 and Production Area of Advance (AoA) at Chalmers University of Technology. We would like to acknowledge the Facility for Analysis, Characterization, Testing and Simulation, Nanyang Technological University, Singapore, for use of their EDS facility.

AUTHOR CONTRIBUTIONS

Conceptualization - S.P.P, V.C., Y.F.L., K.H., and R.V.R; methodology – S.P.P., V.C., Y.F.L., and K.H.; data curation – S.P.P.; formal analysis – S.P.P., V.C., and K.H.; investigation – S.P.P. and V.C.; software– S.P.P., Y.F.L., R.Z., and M.T.; visualization – S.P.P. and K.H.; writing (original draft) – S.P.P.; writing (review and editing) – S.P.P., V.C., Y.F.L., K.H., and R.V.R.; supervision – V.C., Y.F.L., K.H., and R.V.R.; funding acquisition – R.V.R.

DECLARATION OF INTERESTS

The authors declare no competing interests.

Received: January 4, 2024
Revised: March 11, 2024
Accepted: April 8, 2024
Published: April 10, 2024

REFERENCES

1. Gao, C., Min, X., Fang, M., Tao, T., Zheng, X., Liu, Y., Wu, X., and Huang, Z. (2021). Innovative Materials Science via Machine Learning. Adv. Funct. Mater. *32*, 2108044. https://doi.org/10.1002/adfm.202108044.
2. Gutfleisch, O., Willard, M.A., Brück, E., Chen, C.H., Sankar, S.G., and Liu, J.P. (2011). Magnetic materials and devices for the 21st century: stronger, lighter, and more energy efficient. Adv. Mater. *23*, 821–842. https://doi.org/10.1002/adma.201002180.
3. Agrawal, A., and Choudhary, A. (2016). Perspective: Materials informatics and big data: Realization of the "fourth paradigm" of science in materials science. Apl. Mater. *4*, 053208. https://doi.org/10.1063/1.4946894.
4. Wei, J., Chu, X., Sun, X.Y., Xu, K., Deng, H.X., Chen, J., Wei, Z., and Lei, M. (2019). Machine learning in materials science. InfoMat *1*, 338–358. https://doi.org/10.1002/inf2.12028.
5. Himanen, L., Geurts, A., Foster, A.S., and Rinke, P. (2019). Data-Driven Materials Science: Status, Challenges, and Perspectives. Adv. Sci. *6*, 1900808. https://doi.org/10.1002/advs.201900808.
6. Pyzer-Knapp, E.O., Pitera, J.W., Staar, P.W.J., Takeda, S., Laino, T., Sanders, D.P., Sexton, J., Smith, J.R., and Curioni, A. (2022). Accelerating materials discovery using artificial intelligence, high performance computing and robotics. NPJ Comput. Mater. *8*, 84. https://doi.org/10.1038/s41524-022-00765-z.
7. Juan, Y., Dai, Y., Yang, Y., and Zhang, J. (2021). Accelerating materials discovery using machine learning. J. Mater. Sci. Technol. *79*, 178–190. https://doi.org/10.1016/j.jmst.2020.12.010.
8. Conduit, B.D., Jones, N.G., Stone, H.J., and Conduit, G.J. (2017). Design of a nickel-base superalloy using a neural network. Mater. Des. *131*, 358–365. https://doi.org/10.1016/j.matdes.2017.06.007.
9. Correa-Baena, J.-P., Hippalgaonkar, K., van Duren, J., Jaffer, S., Chandrasekhar, V.R., Stevanovic, V., Wadia, C., Guha, S., and Buonassisi, T. (2018). Accelerating Materials Development via Automation, Machine Learning, and High-Performance Computing. Joule *2*, 1410–1420. https://doi.org/10.1016/j.joule.2018.05.009.
10. Westermayr, J., Gastegger, M., Schütt, K.T., and Maurer, R.J. (2021). Perspective on integrating machine learning into computational chemistry and materials science. J. Chem. Phys. *154*, 230903. https://doi.org/10.1063/5.0047760.
11. Pilania, G. (2021). Machine learning in materials science: From explainable predictions to autonomous design. Comput. Mater. Sci. *193*, 110360. https://doi.org/10.1016/j.commatsci.2021.110360.
12. Mishin, Y. (2021). Machine-learning interatomic potentials for materials science. Acta Mater. *214*, 116980. https://doi.org/10.1016/j.actamat.2021.116980.
13. Hart, G.L.W., Mueller, T., Toher, C., and Curtarolo, S. (2021). Machine learning for alloys. Nat. Rev. Mater. *6*, 730–755. https://doi.org/10.1038/s41578-021-00340-w.
14. Liu, X., Xu, P., Zhao, J., Lu, W., Li, M., and Wang, G. (2022). Material machine learning for alloys: Applications, challenges and perspectives. J. Alloys Compd. *921*, 165984. https://doi.org/10.1016/j.jallcom.2022.165984.
15. Batra, R., Song, L., and Ramprasad, R. (2020). Emerging materials intelligence ecosystems propelled by machine learning. Nat. Rev. Mater. *6*, 655–678. https://doi.org/10.1038/s41578-020-00255-y.
16. Butler, K.T., Davies, D.W., Cartwright, H., Isayev, O., and Walsh, A. (2018). Machine learning for molecular and materials science. Nature *559*, 547–555. https://doi.org/10.1038/s41586-018-0337-2.
17. Ludwig, A. (2019). Discovery of new materials using combinatorial synthesis and high-throughput characterization of thin-film materials libraries combined with computational methods. NPJ Comput. Mater. *5*, 70. https://doi.org/10.1038/s41524-019-0205-0.
18. Azumi, K., and Goldman, J.E. (1954). Volume Magnetostriction in Nickel and the Bethe-Slater Interaction Curve. Phys. Rev. *93*, 630–631. https://doi.org/10.1103/PhysRev.93.630.
19. Curtarolo, S., Hart, G.L.W., Nardelli, M.B., Mingo, N., Sanvito, S., and Levy, O. (2013). The high-throughput highway to computational materials design. Nat. Mater. *12*, 191–201. https://doi.org/10.1038/nmat3568.
20. Tao, H., Wu, T., Aldeghi, M., Wu, T.C., Aspuru-Guzik, A., and Kumacheva, E. (2021). Nanoparticle synthesis assisted by machine learning. Nat. Rev. Mater. *6*, 701–716. https://doi.org/10.1038/s41578-021-00337-5.
21. Tabor, D.P., Roch, L.M., Saikin, S.K., Kreisbeck, C., Sheberla, D., Montoya, J.H., Dwaraknath, S., Aykol, M., Ortiz, C., Tribukait, H., et al. (2018). Accelerating the discovery of materials for clean energy in the era of smart automation. Nat. Rev. Mater. *3*, 5–20. https://doi.org/10.1038/s41578-018-0005-z.
22. Silveyra, J.M., Ferrara, E., Huber, D.L., and Monson, T.C. (2018). Soft magnetic materials for a sustainable and electrified world. Science *362*, eaao0195. https://doi.org/10.1126/science.aao0195.
23. Chaudhary, V., Mantri, S.A., Ramanujan, R.V., and Banerjee, R. (2020). Additive manufacturing of magnetic materials. Prog. Mater. Sci. *114*, 100688. https://doi.org/10.1016/j.pmatsci.2020.100688.
24. van Dover, R.B. (2005). Magnetic Materials. Encyclopedia of RF and Microwave Engineering.
25. Gibbs, M.R.J., Hill, E.W., and Wright, P.J. (2004). Magnetic materials for MEMS applications. J. Phys. D Appl. Phys. *37*, R237–R244. https://doi.org/10.1088/0022-3727/37/22/r01.
26. IEA (2021). Electricity Information: Overview. https://www.iea.org/reports/electricity-information-overview.
27. McKinsey & Company (2022). Global Energy Perspective 2022. https://www.mckinsey.com/industries/oil-and-gas/our-insights/global-energy-perspective-2022.
28. Byerly, K., Ohodnicki, P.R., Moon, S.R., Leary, A.M., Keylin, V., McHenry, M.E., Simizu, S., Beddingfield, R., Yu, Y., Feichter, G., et al. (2018). Metal Amorphous Nanocomposite (MANC) Alloy Cores with Spatially Tuned Permeability for Advanced Power Magnetics Applications. JOM *70*, 879–891. https://doi.org/10.1007/s11837-018-2857-5.
29. Patel, P., and Gutfleisch, O. (2018). Advanced magnetic materials could drive next-generation energy technologies. MRS Bull. *43*, 918–919. https://doi.org/10.1557/mrs.2018.300.
30. Aronhime, N., Ohodnicki, P., and McHenry, M.E. (2019). Virtual bound states elements and their effects on magnetic and electrical properties of Fe-Ni based metal amorphous nanocomposites. Scripta Mater. *169*, 9–13. https://doi.org/10.1016/j.scriptamat.2019.05.003.
31. Henke, M., Narjes, G., Hoffmann, J., Wohlers, C., Urbanek, S., Heister, C., Steinbrink, J., Canders, W.-R., and Ponick, B. (2018). Challenges and Opportunities of Very Light High-Performance Electric Drives for Aviation. Energies *11*, 344.
32. Moreels, D., and Leijnen, P. (2019). Turning the electric motor inside out: A Belgian startup's axial-flux motor for EVs is small, light, and powerful. IEEE Spectr. *56*, 40–45. https://doi.org/10.1109/mspec.2019.8847589.
33. Padhy, S.P., Tsakadze, Z., Chaudhary, V., Lim, G.J., Tan, X., Lew, W.S., and Ramanujan, R.V. (2022). Rapid multi-property assessment of compositionally modulated Fe-Co-Ni thin film material libraries. Results Materials *14*, 100283. https://doi.org/10.1016/j.rinma.2022.100283.
34. Han, L., Maccari, F., Souza Filho, I.R., Peter, N.J., Wei, Y., Gault, B., Gutfleisch, O., Li, Z., and Raabe, D. (2022). A mechanically strong and ductile soft magnet with extremely low coercivity. Nature *608*, 310–316. https://doi.org/10.1038/s41586-022-04935-3.
35. George, E.P. (2022). Magnetically Soft but Mechanically Tough Alloys (Nature Publishing Group).
36. McHenry, M.E., and Laughlin, D.E. (2014). Magnetic Properties of Metals and Alloys. In Physical Metallurgy, D.E. Laughlin and K. Hono, eds. (Elsevier), pp. 1881–2008. https://doi.org/10.1016/b978-0-444-53770-6.00019-8.
37. Yang, F., Li, Z., Wang, Q., Jiang, B., Yan, B., Zhang, P., Xu, W., Dong, C., and Liaw, P.K. (2020). Cluster-formula-embedded machine learning for design of multicomponent β-Ti

alloys with low Young's modulus. NPJ Comput. Mater. *6*, 101. https://doi.org/10.1038/s41524-020-00372-w.

38. Wen, C., Zhang, Y., Wang, C., Xue, D., Bai, Y., Antonov, S., Dai, L., Lookman, T., and Su, Y. (2019). Machine learning assisted design of high entropy alloys with desired property. Acta Mater. *170*, 109–117. https://doi.org/10.1016/j.actamat.2019.03.010.
39. Zeng, Y., Man, M., Ng, C.K., Wuu, D., Lee, J.J., Wei, F., Wang, P., Bai, K., Cheh Tan, D.C., and Zhang, Y.-W. (2022). Machine learning-based inverse design for single-phase high entropy alloys. Apl. Mater. *10*. https://doi.org/10.1063/5.0109491.
40. Yang, C., Ren, C., Jia, Y., Wang, G., Li, M., and Lu, W. (2022). A machine learning-based alloy design system to facilitate the rational design of high entropy alloys with enhanced hardness. Acta Mater. *222*, 117431. https://doi.org/10.1016/j.actamat.2021.117431.
41. Conduit, B.D., Jones, N.G., Stone, H.J., and Conduit, G.J. (2018). Probabilistic design of a molybdenum-base alloy using a neural network. Scripta Mater. *146*, 82–86. https://doi.org/10.1016/j.scriptamat.2017.11.008.
42. Conduit, B.D., Illston, T., Baker, S., Duggappa, D.V., Harding, S., Stone, H.J., and Conduit, G.J. (2019). Probabilistic neural network identification of an alloy for direct laser deposition. Mater. Des. *168*, 107644. https://doi.org/10.1016/j.matdes.2019.107644.
43. Wang, Y., Tian, Y., Kirk, T., Laris, O., Ross, J.H., Noebe, R.D., Keylin, V., and Arróyave, R. (2020). Accelerated design of Fe-based soft magnetic materials using machine learning and stochastic optimization. Acta Mater. *194*, 144–155. https://doi.org/10.1016/j.actamat.2020.05.006.
44. Liu, P., Huang, H., Antonov, S., Wen, C., Xue, D., Chen, H., Li, L., Feng, Q., Omori, T., and Su, Y. (2020). Machine learning assisted design of γ'-strengthened Co-base superalloys with multi-performance optimization. NPJ Comput. Mater. *6*, 62. https://doi.org/10.1038/s41524-020-0334-5.
45. Zhang, H., Fu, H., Shen, Y., and Xie, J. (2022). Rapid design of secondary deformation-aging parameters for ultra-low Co content Cu-Ni-Co-Si-X alloy via Bayesian optimization machine learning. Int. J. Miner. Metall. Mater. *29*, 1197–1205. https://doi.org/10.1007/s12613-022-2479-3.
46. Zhang, J., Cai, C., Kim, G., Wang, Y., and Chen, W. (2022). Composition design of high-entropy alloys with deep sets learning. NPJ Comput. Mater. *8*, 89. https://doi.org/10.1038/s41524-022-00779-7.
47. Tang, Y., Wan, Y., Wang, Z., Zhang, C., Han, J., Hu, C., and Tang, C. (2022). Machine learning and Python assisted design and verification of Fe–based amorphous/nanocrystalline alloy. Mater. Des. *219*, 110726. https://doi.org/10.1016/j.matdes.2022.110726.
48. The Pandas Development Team (2020 (pandas-dev/pandas: Pandas. Zenodo).
49. McKinney, W. (2010). Data structures for statistical computing in python, pp. 51–56. 1. held in Austin, TX.
50. McKinney, W. (2011). pandas: a foundational Python library for data analysis and statistics. In Python for high performance and scientific computing, 14Python for high performance and scientific computing, pp. 1–9.
51. Hunter, J.D. (2007). Matplotlib: A 2D Graphics Environment. Comput. Sci. Eng. *9*, 90–95. https://doi.org/10.1109/mcse.2007.55.
52. Waskom, M. (2021). seaborn: statistical data visualization. J. Open Source Softw. 6, 3021.
53. Plotly Technologies Inc (2015). Collaborative Data Science. Plotly Technologies Inc.
54. Chollet, F. others. (2015). Keras. GitHub. https://keras.io/getting_started/faq/#how-should-i-cite-keras.
55. Abadi, M., Barham, P., Chen, J., Chen, Z., Davis, A., Dean, J., Devin, M., Ghemawat, S., Irving, G., Isard, M., et al. (2016). TensorFlow: a system for large-scale machine learning. In Proceedings of the 12th USENIX Conference on Operating Systems Design and Implementation (USENIX Association).
56. Chen, T., and Guestrin, C. (2016). Xgboost: A Scalable Tree Boosting System, pp. 785–794.
57. Pedregosa, F., Varoquaux, G., Gramfort, A., Michel, V., Thirion, B., Grisel, O., Blondel, M., Prettenhofer, P., Weiss, R., and Dubourg, V. (2011). Scikit-learn: Machine learning in Python. J. Mach. Learn. Res. *12*, 2825–2830.
58. Head, T., Kumar, M., Nahrstaedt, H., Louppe, G., and Shcherbatyi, I. (2021). Scikit-Optimize (Zenodo).
59. Padhy, S.P., Chaudhary, V., Lim, Y.F., Zhu, R., Thway, M., Hippalgaonkar, K., and Ramanujan, R.V. (2024). Data-and-Codes-for-Experimentally-Validated-Inverse-design-of-Multi-Property-Fe-Co-Ni-alloys: Data and codes release. Zenodo *v1.0.1*. https://doi.org/10.5281/zenodo.10686272.
60. Bozorth, R.M. (1993). Ferromagnetism (Wiley-IEEE Press).
61. Coey, J.M.D. (2012). Magnetism and Magnetic Materials (Cambridge university press). https://doi.org/10.1017/cbo9780511845000.
62. Connolly, T.F., and Copenhaver, E.D. (1972). Bibliography of Magnetic Materials and Tabulation of Magnetic Transition Temperatures (Springer Science & Business Media). https://doi.org/10.1007/978-1-4684-1396-0.
63. Beiss, P., Ruthardt, R., and Warlimont, H. (2003). Powder Metallurgy Data Part 1: Metal and Magnets (Springer).
64. ASM Handbook Volume 2: Properties and Selection: Nonferrous Alloys and Special Purpose Materials (1990 (ASM International).
65. Kutz, M. (2002). Handbook of Materials Selection (John Wiley & Sons). https://doi.org/10.1002/9780470172551.
66. Bassford, T.H., and Hosier, J. (2002). Nickel and Its Alloys. In Handbook of Materials Selection (John Wiley & Sons), pp. 235–258. https://doi.org/10.1002/9780470172551.ch7.
67. Elmen, G.W. (1936). Magnetic Alloys of Iron, Nickel, and Cobalt. Bell Syst. Tech. J. *15*, 113–135. https://doi.org/10.1002/j.1538-7305.1936.tb00721.x.
68. Wohlfabth, E.P. (2010). CI. Magnetic properties of nickel-cobalt and related alloys. London, Edinburgh Dublin Phil. Mag. J. Sci. *40*, 1095–1111. https://doi.org/10.1080/14786444908521747.
69. Sussman, H., and Ehrlich, S.L. (1950). Evaluation of the Magnetostrictive Properties of Hiperco. J. Acoust. Soc. Am. *22*, 499–506. https://doi.org/10.1121/1.1906634.
70. Smit, J. (1955). The spontaneous hall effect in ferromagnetics I. Physica *21*, 877–887. https://doi.org/10.1016/s0031-8914(55)92596-9.
71. Parsons, D., Sucksmith, W., and Thompson, J.E. (1958). The magnetization of cobalt-aluminium, cobalt-silicon, iron-aluminium and iron-silicon alloys. Phil. Mag. *3*, 1174–1184. https://doi.org/10.1080/14786435808237047.
72. Van Elst, H.C. (1959). The anisotropy in the magneto-resistance of some nickel alloys. Physica *25*, 708–720. https://doi.org/10.1016/s0031-8914(59)97412-9.
73. Shull, D.S. (1961). Improved Magnetic Properties of High-Purity Iron-Cobalt Alloys Containing 27–43% Cobalt. J. Appl. Phys. *32*, S356–S357. https://doi.org/10.1063/1.2000466.
74. Chen, C.W. (1962). Saturation moments and residual resistivities of iron-cobalt ternary alloys. Phil. Mag. *7*, 1753–1764. https://doi.org/10.1080/14786436208213707.
75. Crangle, J., Hallam, G.C., and Sucksmith, W. (1997). The magnetization of face-centred cubic and body-centred cubic iron + nickel alloys. Proc. R. Soc. Lond. A Math. Phys. Sci. *272*, 119–132. https://doi.org/10.1098/rspa.1963.0045.
76. Fraser, R.W., and Evans, D.J.I. (2014). The Properties of Cobalt–Iron Alloys Prepared by Powder Rolling. Powder Metall. *11*, 358–378. https://doi.org/10.1179/pom.1968.11.22.009.
77. Chin, G.Y., Nesbitt, E.A., Wernick, J.H., and Mendorf, D.R. (1969). Medium-Coercive-Force Permanent-Magnet Alloys Based on the Co–Fe–Ti System. J. Appl. Phys. *40*, 760–763. https://doi.org/10.1063/1.1657461.
78. Colling, D.A. (1969). Intrinsic Magnetization of Fe–Ni–Mn Alloys. J. Appl. Phys. *40*, 1379–1381. https://doi.org/10.1063/1.1657677.
79. Thornburg, D.R. (1969). High-Strength High-ductility Cobalt-Iron Alloys. J. Appl. Phys. *40*, 1579–1580. https://doi.org/10.1063/1.1657779.
80. Tracey, V.A., and Raman, R.S.K. (2014). The Mechanical Properties of Some Sintered Maraging Steels. Powder Metall. *12*, 131–156. https://doi.org/10.1179/pom.1969.12.23.006.
81. Sasaki, T., Okada, M., Kassai, M., and Henmi, Z. (1970). Semihard Magnetic Alloys of Co–Fe–Nb System. J. Appl. Phys. *41*, 1105–1106. https://doi.org/10.1063/1.1658833.
82. Chin, G.Y., Tisone, T.C., and Grupen, W.B. (1971). Metallurgical Control of Magnetic Properties in Co–Fe and Ni–Fe Alloys for Memory Applications. J. Appl. Phys. *42*, 1502–1509. https://doi.org/10.1063/1.1660320.
83. Kassai, M., Okada, M., Sasaki, T., and Henmi, Z. (1972). Magnetic Anisotropy of a Semihard Magnetic Alloy of the Co–Fe–Nb System. Trans. Indian Inst. Met. *13*, 385–390. https://doi.org/10.2320/matertrans1960.13.385.
84. Marikar, Y., and Vasu, K.I. (1974). Electrodeposition of the ternary iron-cobalt-nickel alloy from the fluoborate bath part II. Structure and properties of the deposits. Electrodepos. Surf. Treat. *2*, 295–302. https://doi.org/10.1016/0300-9416(74)90005-4.
85. Kawahara, K., and Uehara, M. (1984). A possibility for developing high strength soft magnetic materials in FeCo-X alloys.

J. Mater. Sci. *19*, 2575–2581. https://doi.org/10.1007/bf00550812.

86. Achilleos, C.A., Kyprianidis, I.M., and Tsoukalas, I.A. (1991). On the magnetic properties and $\alpha \leftrightarrow \lambda$ transformation of some Fe Co Ni ternary alloys. Solid State Commun. *79*, 209–216. https://doi.org/10.1016/0038-1098(91)90636-a.
87. Achilleos, C.A., Chadjivasiliou, S.C., and Tsoukalas, I.A. (1991). On the electrical properties and $\alpha \leftrightarrows \gamma$ transformation of some Fe Co Ni ternary alloys. Mater. Res. Bull. *26*, 821–834. https://doi.org/10.1016/0025-5408(91)90072-t.
88. Jen, S.U., Chiang, H.P., Chung, C.M., and Kao, M.N. (2001). Magnetic properties of Co–Fe–Ni films. J. Magn. Magn Mater. *236*, 312–319. https://doi.org/10.1016/s0304-8853(01)00457-7.
89. Wang, L., Gao, Y., Xue, Q., Liu, H., and Xu, T. (2005). Microstructure and tribological properties of electrodeposited Ni–Co alloy deposits. Appl. Surf. Sci. *242*, 326–332. https://doi.org/10.1016/j.apsusc.2004.08.033.
90. Srivastava, M., Ezhil Selvi, V., William Grips, V.K., and Rajam, K.S. (2006). Corrosion resistance and microstructure of electrodeposited nickel–cobalt alloy coatings. Surf. Coating. Technol. *201*, 3051–3060. https://doi.org/10.1016/j.surfcoat.2006.06.017.
91. Tóth, B.G., Péter, L., Révész, Á., Pádár, J., and Bakonyi, I. (2010). Temperature dependence of the electrical resistivity and the anisotropic magnetoresistance (AMR) of electrodeposited Ni-Co alloys. Eur. Phys. J. B *75*, 167–177. https://doi.org/10.1140/epjb/e2010-00132-4.
92. Karpuz, A., Kockar, H., Alper, M., Karaagac, O., and Haciismailoglu, M. (2012). Electrodeposited Ni–Co films from electrolytes with different Co contents. Appl. Surf. Sci. *258*, 4005–4010. https://doi.org/10.1016/j.apsusc.2011.12.088.
93. Sourmail, T. (2005). Near equiatomic FeCo alloys: Constitution, mechanical and magnetic properties. Prog. Mater. Sci. *50*, 816–880. https://doi.org/10.1016/j.pmatsci.2005.04.001.
94. Fingers, R.T., and Kozlowski, G. (1997). Microstructure and magnetic properties of Fe–Co alloys. J. Appl. Phys. *81*, 4110–4111. https://doi.org/10.1063/1.365095.
95. Yu, R.H., Basu, S., Ren, L., Zhang, Y., Parvizi-Majidi, A., Unruh, K.M., and Xiao, J.Q. (2000). High temperature soft magnetic materials: FeCo alloys and composites. IEEE Trans. Magn. *36*, 3388–3393. https://doi.org/10.1109/20.908809.
96. Yu, R.H., Basu, S., Zhang, Y., and Xiao, J.Q. (1999). Magnetic domains and coercivity in FeCo soft magnetic alloys. J. Appl. Phys. *85*, 6034–6036. https://doi.org/10.1063/1.369073.
97. Geist, B., Peterson, T., Horwath, J.C., Turgut, Z., Huang, M.Q., Snyder, R.A., and Fingers, R.T. (2003). Effect of high-temperature aging on electrical properties of Hiperco®27, Hiperco®50, and Hiperco®50 HS alloys. J. Appl. Phys. *93*, 6686–6688. https://doi.org/10.1063/1.1556104.
98. Thomas, B. (1980). The influence of nickel on the magnetic and mechanical properties of Co-Fe-V alloy. IEEE Trans. Magn. *16*, 444–454. https://doi.org/10.1109/tmag.1980.1060594.
99. Persiano, A.I.C., and Rawlings, R.D. (1991). Effect of niobium additions on the structure and magnetic properties of equiatomic iron-cobalt alloys. J. Mater. Sci. *26*, 4026–4032. https://doi.org/10.1007/bf02402943.
100. Hailer, B.T. (2001). Effect of Heat Treatment on Magnetic and Mechanical Properties of an Iron-Cobalt-Vanadium-Niobium Alloy (Virginia Tech).
101. Sundar, R.S., Deevi, S.C., and Reddy, B.V. (2005). High Strength FeCo–V Intermetallic Alloy: Electrical and Magnetic Properties. J. Mater. Res. *20*, 1515–1522. https://doi.org/10.1557/jmr.2005.0206.
102. Nagayama, T., Yamamoto, T., and Nakamura, T. (2016). Thermal expansions and mechanical properties of electrodeposited Fe–Ni alloys in the Invar composition range. Electrochim. Acta *205*, 178–187. https://doi.org/10.1016/j.electacta.2016.04.089.
103. Matsui, I., Kawakatsu, T., Takigawa, Y., Uesugi, T., and Higashi, K. (2014). Fabrication of bulk nanocrystalline Fe–Ni alloys with high strength and high ductility by an electrodeposition. Mater. Lett. *116*, 71–74. https://doi.org/10.1016/j.matlet.2013.10.108.
104. Mehrizi, S., and Heydarzadeh Sohi, M. (2015). Electrical resistivity and magnetic properties of electrodeposited nanocrystalline CoFe thin films. J. Mater. Sci. Mater. Electron. *26*, 7381–7389. https://doi.org/10.1007/s10854-015-3368-6.
105. Ahmad, S., Ziya, A.B., Ashiq, M.N., Ibrahim, A., Atiq, S., Ahmad, N., Shakeel, M., and Khan, M.A. (2016). Improved magnetic and electrical properties of Cu doped Fe–Ni invar alloys synthesized by chemical reduction technique. J. Magn. Magn Mater. *419*, 125–130. https://doi.org/10.1016/j.jmmm.2016.06.033.
106. Mikler, C.V., Chaudhary, V., Borkar, T., Soni, V., Choudhuri, D., Ramanujan, R.V., and Banerjee, R. (2017). Laser additive processing of Ni-Fe-V and Ni-Fe-Mo Permalloys: Microstructure and magnetic properties. Mater. Lett. *192*, 9–11. https://doi.org/10.1016/j.matlet.2017.01.059.
107. Mikler, C.V., Chaudhary, V., Soni, V., Gwalani, B., Ramanujan, R.V., and Banerjee, R. (2017). Tuning the phase stability and magnetic properties of laser additively processed Fe-30at%Ni soft magnetic alloys. Mater. Lett. *199*, 88–92. https://doi.org/10.1016/j.matlet.2017.04.054.
108. Kustas, A.B., Susan, D.F., Johnson, K.L., Whetten, S.R., Rodriguez, M.A., Dagel, D.J., Michael, J.R., Keicher, D.M., and Argibay, N. (2018). Characterization of the Fe-Co-1.5V soft ferromagnetic alloy processed by Laser Engineered Net Shaping (LENS). Addit. Manuf. *21*, 41–52. https://doi.org/10.1016/j.addma.2018.02.006.
109. Chaudhary, V., Sai Kiran Kumar Yadav, N.M., Mantri, S.A., Dasari, S., Jagetia, A., Ramanujan, R.V., and Banerjee, R. (2020). Additive manufacturing of functionally graded Co–Fe and Ni–Fe magnetic materials. J. Alloys Compd. *823*, 153817. https://doi.org/10.1016/j.jallcom.2020.153817.
110. Mazeeva, A.K., Staritsyn, M.V., Bobyr, V.V., Manninen, S.A., Kuznetsov, P.A., and Klimov, V.N. (2020). Magnetic properties of Fe–Ni permalloy produced by selective laser melting. J. Alloys Compd. *814*, 152315. https://doi.org/10.1016/j.jallcom.2019.152315.
111. Yanai, T., Mieda, K., Kaji, J., Tanaka, R., Yamashita, A., Morimura, T., Nakano, M., and Fukunaga, H. (2020). Electroplated Fe-Co films prepared in citric-acid-based plating baths with saccharin and sodium lauryl sulfate. AIP Adv. *10*, 055001. https://doi.org/10.1063/1.5130468.
112. Chaudhary, V., Tan, L.P., Sharma, V.K., and Ramanujan, R.V. (2021). Accelerated study of magnetic Fe-Co-Ni alloys through compositionally graded spark plasma sintered samples. J. Alloys Compd. *869*, 159318. https://doi.org/10.1016/j.jallcom.2021.159318.
113. Mitchell, M., Muftakhidinov, B., Winchen, T., Wilms, A., Schaik, B.v., Mo-Gul, Badger, T.G., and Jędrzejewski-Szmek, Z.; kensington, and kylesower (2020). Enguage Digitzer Software. http://markummitchell.github.io/engauge-digitizer.
114. Wikipedia (2022). Prices of Chemical Elements. https://en.wikipedia.org/wiki/Prices_of_chemical_elements.
115. Cort, J.W., and Kenji, M. (2005). Advantages of the mean absolute error (MAE) over the root mean square error (RMSE) in assessing average model performance. Clim. Res. *30*, 79–82.
116. Greenhill, S., Rana, S., Gupta, S., Vellanki, P., and Venkatesh, S. (2020). Bayesian Optimization for Adaptive Experimental Design: A Review. IEEE Access *8*, 13937–13948. https://doi.org/10.1109/ACCESS.2020.2966228.
117. Herbol, H.C., Poloczek, M., and Clancy, P. (2020). Cost-effective materials discovery: Bayesian optimization across multiple information sources. Mater. Horiz. *7*, 2113–2123. https://doi.org/10.1039/D0MH00062K.
118. Frazier, P.I., and Wang, J. (2016). Bayesian Optimization for Materials Design. In Information Science for Materials Discovery and Design, T. Lookman, F.J. Alexander, and K. Rajan, eds. (Springer International Publishing), pp. 45–75. https://doi.org/10.1007/978-3-319-23871-5_3.
119. Frazier, P.I. (2018). A tutorial on Bayesian optimization. Preprint at arXiv. https://doi.org/10.48550/arXiv.1807.02811.
120. Brochu, E., Cora, V.M., and De Freitas, N. (2010). A tutorial on Bayesian optimization of expensive cost functions, with application to active user modeling and hierarchical reinforcement learning. Preprint at arXiv. https://doi.org/10.48550/arXiv.1012.2599.
121. Padhy, S.P., Tan, L.P., Varma, V.B., Chaudhary, V., Tsakadze, Z., and Ramanujan, R.V. (2023). Accelerated Multi-Property Screening of Fe-Co-Ni Alloy Libraries by Hyper-Heuristic Combinatorial Flow Synthesis and High-Throughput Spark Plasma Sintering. J. Mater. Res. Technol. *27*, 2976–2988. https://doi.org/10.1016/j.jmrt.2023.10.124.
122. Tan, L.P., Padhy, S.P., Tsakadze, Z., Chaudhary, V., and Ramanujan, R.V. (2022). Accelerated property evaluation of Ni–Co materials libraries produced by multiple processing techniques. J. Mater. Res. Technol. *20*, 4186–4196. https://doi.org/10.1016/j.jmrt.2022.08.152.
123. Teh, W.H., Chaudhary, V., Chen, S., Lim, S.H., Wei, F., Lee, J.Y., Wang, P., Padhy, S.P., Tan, C.C., and Ramanujan, R.V. (2022). High throughput multi-property evaluation of additively manufactured Co-Fe-Ni materials libraries. Addit. Manuf. *58*, 102983. https://doi.org/10.1016/j.addma.2022.102983.

124. Myers, H.P., and Sucksmith, W. (1997). The spontaneous magnetization of cobalt. Proc. R. Soc. Lond. A Math. Phys. Sci. *207*, 427–446. https://doi.org/10.1098/rspa.1951.0132.
125. Legendre, B., and Sghaier, M. (2011). Curie temperature of nickel. J. Therm. Anal. Calorim. *105*, 141–143. https://doi.org/10.1007/s10973-011-1448-2.
126. Chaudhary, V., and Ramanujan, R.V. (2016). Magnetocaloric Properties of Fe-Ni-Cr Nanoparticles for Active Cooling. Sci. Rep. *6*, 35156. https://doi.org/10.1038/srep35156.
127. Kauwe, S.K., Graser, J., Murdock, R., and Sparks, T.D. (2020). Can machine learning find extraordinary materials? Comput. Mater. Sci. *174*, 109498. https://doi.org/10.1016/j.commatsci.2019.109498.
128. Xiong, Z., Cui, Y., Liu, Z., Zhao, Y., Hu, M., and Hu, J. (2020). Evaluating explorative prediction power of machine learning algorithms for materials discovery using k-fold forward cross-validation. Comput. Mater. Sci. *171*, 109203. https://doi.org/10.1016/j.commatsci.2019.109203.
129. Ward, L., Dunn, A., Faghaninia, A., Zimmermann, N.E., Bajaj, S., Wang, Q., Montoya, J., Chen, J., Bystrom, K., Dylla, M., et al. (2018). Matminer: An open source toolkit for materials data mining. Comput. Mater. Sci. *152*, 60–69. https://doi.org/10.1016/j.commatsci.2018.05.018.
130. Moses, A. (1990). Electrical steels: past, present and future developments. IEE Proceedings A (Physical Science, Measurement and Instrumentation. Manag. Educ. *137*, 233–245.
131. ThyssenKrupp AG Powercore® C. https://www.thyssenkrupp-steel.com/en/products/electrical-steel/electrical-steel-grain-oriented/powercore-c/typical-physical-properties/content-page-71.html.
132. Kasai, S., Namikawa, M., and Hiratani, T. (2016). Recent Progress of High Silicon Electrical Steel in JFE Steel. JFE Steel Corporation, Tokyo, Japan. JFE Tech. Rep. *21*.
133. Abe, M., Takada, Y., Murakami, T., Tanaka, Y., and Mihara, Y. (1989). Magnetic properties of commercially produced Fe-6.5wt% Si sheet. J. Mater. Eng. *11*, 109–116. https://doi.org/10.1007/BF02833761.
134. Fiorillo, F., Bertotti, G., Appino, C., and Pasquale, M. (2000). Soft Magnetic Materials. In Wiley Encyclopedia of Electrical and Electronics Engineering, pp. 1–42. https://doi.org/10.1002/047134608X.W4504.pub2.
135. Tan, L.P., Chaudhary, V., Tsakadze, Z., and Ramanujan, R.V. (2022). Rapid multiple property determination from bulk materials libraries prepared from chemically synthesized powders. Sci. Rep. *12*, 9504. https://doi.org/10.1038/s41598-022-13691-3.
136. NiWire Industries Permalloy. https://www.niwire.com/uploads/documents/Permalloy%20Wire_Strip_Bar.pdf.
137. ASTM International (2021). ASTM A753 - Standard Specification for Wrought Nickel-Iron Soft Magnetic Alloys (UNS K94490, K94840, N14076, N14080).
138. Special Metals The NILO® and NILOMAG® Nickel-Iron Alloys. https://www.specialmetals.com/documents/technical-bulletins/nilo-alloys.pdf.

STAR★METHODS

KEY RESOURCES TABLE

REAGENT or RESOURCE	SOURCE	IDENTIFIER
Deposited data		
GitHub repository with literature curated and experimental data and code (https://github.com/Shakti-95/Data-and-Codes-for-Experimentally-Validated-Inverse-design-of-Multi-Property-Fe-Co-Ni-alloys)	This paper; Zenodo	https://doi.org/10.5281/zenodo.10686272
Software and algorithms		
Python 3.9	Python Software Foundation	https://www.python.org/
Jupyter notebook	Jupyter	https://jupyter.org/
WenAlloys featurizer (Matminer)	Wen et al.,[38] 2019	https://doi.org/10.1016/j.actamat.2019.03.010

RESOURCE AVAILABILITY

Lead contact

Further information and requests for resources should be directed to the lead contact, Prof. Raju V. Ramanujan (ramanujan@ntu.edu.sg).

Materials availability

This study did not generate new materials.

Data and code availability

- The curated data from literature, imputed data, and experimental data have been deposited in the GitHub repository (https://github.com/Shakti-95/Data-and-Codes-for-Experimentally-Validated-Inverse-design-of-Multi-Property-Fe-Co-Ni-alloys) and are publicly available.
- All original codes have been deposited in the GitHub repository (https://github.com/Shakti-95/Data-and-Codes-for-Experimentally-Validated-Inverse-design-of-Multi-Property-Fe-Co-Ni-alloys) and are publicly available as of the date of publication. DOIs are listed in the key resources table.
- Any additional information required to reanalyze the data reported in this paper is available from the lead contact upon request.

EXPERIMENTAL MODEL AND STUDY PARTICIPANT DETAILS

This work did not need any unique experimental model.

METHOD DETAILS

The complete Methodology section in the main text should be under this section heading.

QUANTIFICATION AND STATISTICAL ANALYSIS

All the analysis and plots were performed in Python. The figures were all prepared using licensed version of Adobe Illustrator.